ac Stark Spectroscopy of Interactions between Moiré Excitons and Polarons

B. Evrard,[1] H. S. Adlong,[1,2] A. A. Ghita,[1] T. Uto,[1] L. Ciorciaro,[1] K. Watanabe,[3] T. Taniguchi,[3] M. Kroner,[1] and A. İmamoğlu[1]

[1]*Institute for Quantum Electronics, ETH Zürich, Zürich, Switzerland*
[2]*Institute for Theoretical Physics, ETH Zürich, Zürich, Switzerland*
[3]*Research Center for Electronic and Optical Materials, NIMS, 1-1 Namiki, Tsukuba 305-0044, Japan*

(Received 26 February 2024; revised 4 November 2024; accepted 4 March 2025; published 1 April 2025)

We use nonlinear pump-probe spectroscopy to study optical excitations in a charge-tunable $MoSe_2/WS_2$ moiré heterostructure. An intense red-detuned laser pulse creates a photonic dressing of the material by introducing a large *virtual* population of excitons or exciton polarons in a deep moiré potential. By measuring the resulting ac Stark effect with a weak resonant laser pulse, we gain access to the nature and mutual interactions of the elementary optical excitations. At charge neutrality, our measurements reveal that different exciton resonances, associated with confinement of their center-of-mass motion in the moiré potential, have a significant spatial overlap. The resulting short-range interactions manifest themselves as a density-dependent blueshift for same-valley excitons and bound biexciton states for opposite-valley excitons. The attractive polaron resonance that appears upon injection of electrons into the heterostructure shows a contrasting behavior: Here, we observe an electron-density-independent light shift and a clear pump-power-dependent saturation. These features are equivalent to that of an ensemble of independent two-level emitters and indicate a breakdown of the Fermi-polaron picture for optical excitations of electrons subject to a strong moiré potential. Our work establishes an experimental approach to elucidate the elementary optical excitations of semiconductor moiré heterostructures, providing a solid ground for the spectroscopy of correlated electronic and excitonic states in such materials.

DOI: 10.1103/PhysRevX.15.021002

Subject Areas: Condensed Matter Physics, Semiconductor Physics, Strongly Correlated Materials

I. INTRODUCTION

Semiconductor moiré materials have emerged as a rich playground for the exploration of strongly correlated electrons [1–3]. In twisted bilayers of transition metal dichalcogenides (TMDs), linear spectroscopy has enabled the observation of a wealth of many-body states, ranging from correlated Mott-Wigner states [4–6], through kinetic magnetism [7] to fractional Chern insulators [8,9]. Indeed, attractive and repulsive exciton polarons, resulting from the dynamical dressing of excitons by itinerant charges [10–15], provide built-in sensors for both the charge and magnetic order of electrons in TMDs [16,17]. Going beyond a mere diagnostic purpose, optical excitations of moiré materials have also been proposed as building blocks of correlated bosonic systems [18–21]. Consequently, a complete characterization of moiré exciton and exciton-polaron resonances is essential for correctly interpreting spectroscopic signatures of a broad set of correlated states in semiconductor moiré materials [22–27].

Here, we use nonlinear ac Stark spectroscopy to measure the interactions and possible bound states arising between different elementary optical excitations of a $MoSe_2/WS_2$ heterostructure. Our approach relies on an intense red-detuned pump beam to generate a significant density of virtual excitations and on a weak broadband probe pulse to monitor the subsequent modification of the optical spectrum. By detuning the pump away from any resonances, we alleviate real-absorption-induced modification of the electronic state and look at the coherent scattering response of the system. In TMD monolayers, repulsive Coulomb exchange interactions between itinerant excitations generated by the pump and the probe result in a blueshift when both lasers are cocircularly polarized [28–35]. For cross-circular polarization, the sign of the light shift depends on the pump frequency: This is a manifestation of an underlying Feshbach resonance, occurring when the pump detuning from the exciton resonance equals the biexciton binding energy [36–40]. Our prior measurements also revealed a striking electron density dependence of the light shift which allowed us to determine a dramatic enhancement of

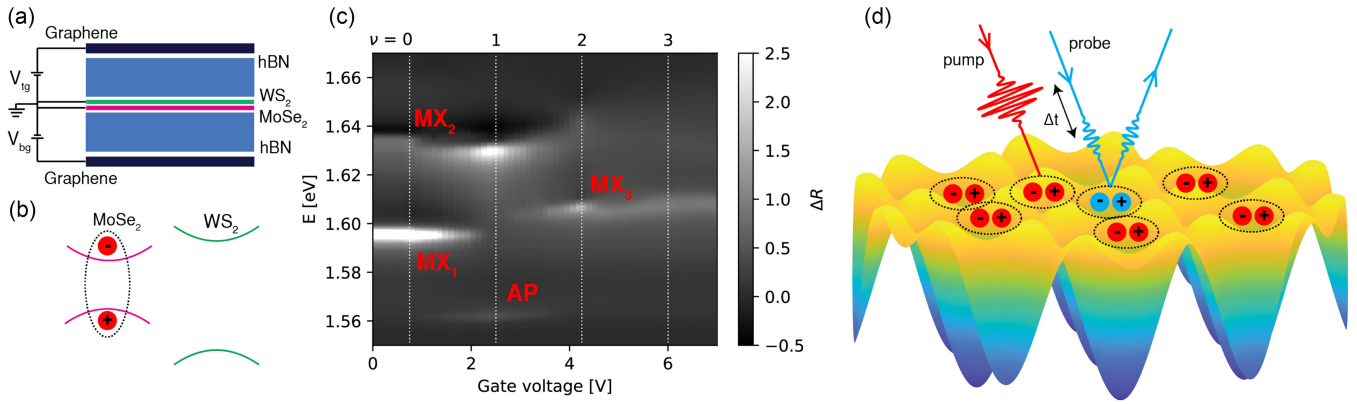

FIG. 1. Overview of the sample and experiment. (a) Schematic of the device. The TMDs $MoSe_2$ and WS_2 form the moiré material that we investigate. It is encapsulated in two approximately 35-nm-thick *h*-BN flakes and dual gated with graphite electrodes to enable an independent control of the chemical potential and electric field. The latter is kept close to zero, such that only $MoSe_2$ is doped at low densities, given the band alignment (b). The evolution of the reflection spectrum of $MoSe_2$ as a function of the electronic density (c) reveals several moiré exciton and polaron resonances, which we investigate. We rely on a pump-probe scheme (d) where an intense red-detuned laser generates a virtual population of moiré excitations. The interaction between this background and a test excitation generated with a probe laser are then measured.

interactions between attractive polarons (APs) [34]. In this work, we employ ac Stark spectroscopy on a TMD bilayer featuring a deep moiré potential to reveal three new features: (i) At charge neutrality where two bright moiré excitons dominate the spectrum, we observe a blueshift of a moiré exciton mode induced by the interaction with the other mode. This interspecies ac Stark effect, with no equivalent in a monolayer TMD, reveals the extent of spatial overlap between the two orthonormal modes. (ii) We identify moiré biexciton Feshbach resonances associated with bound states of both the same and different moiré exciton modes [41]. To explain the nature of these biexciton states, we develop a theoretical model for the scattering of excitons in a moiré potential and find good qualitative agreement with the experiment. (iii) We find that the electron density dependence of the ac Stark shift, as well as the pump-power-dependent saturation, of the AP resonance is qualitatively different from that of a monolayer. Our findings correspond to those of an ensemble of independent two-level emitters, indicating a breakdown of the Fermi-polaron picture for optical excitations of electrons subject to a strong moiré potential.

Our measurements are carried out in a $\simeq 0°$ stacked $MoSe_2/WS_2$ heterostructure, exhibiting a type I band alignment where the lowest (highest) energy moiré conduction (valence) band resides in $MoSe_2$ [Figs. 1(a) and 1(b)]. The electron-density-dependent reflection contrast exhibits four bright resonances, which we identify as MX_1, MX_2, AP, and MX_3 to be consistent with the notation used in an earlier publication [7] [Fig. 1(c)]. A strong pump laser with a finite red detuning from a given resonance generates a large virtual population of the corresponding moiré exciton modes that exists only during the approximately 0.2 ps duration of the pump pulse. We estimate a maximum virtual exciton population in MX_1 of approximately 10^{12} cm^{-2} for a pump detuning of $\delta_1 \approx 20$ meV (for more details, see Appendix E). A weak, broadband probe pulse then measures the energy shift of all excitonic species concurrently [Fig. 1(d)]. Throughout this work, we set the pump laser detuning from the excitonic resonances to be much smaller than the exciton binding energy: In this limit, the dominant contribution to the light shift of the resonances originates from exciton-exciton interactions [28–34]. We determine both intra- and interspecies interaction strengths between the moiré exciton or polaron modes as a function of the electron density by measuring the light shift in this small detuning limit.

II. INTERACTIONS BETWEEN MOIRÉ EXCITONS

We begin by performing nonlinear ac Stark spectroscopy at charge neutrality in order to understand how the moiré potential modifies exciton-exciton interactions and biexcitons. Since the exciton binding energy (Bohr radius) is much larger (smaller) than all other relevant energy (length) scales, the role of the moiré potential is to induce a periodic potential for the center-of-mass motion of the $1s$ exciton [42]. When the moiré potential is weak, we would observe umklapp resonances, blueshifted from the $k = 0$ $1s$ exciton mode by $\simeq (\hbar k_M)^2/(2m_{ex})$, where k_M is the reciprocal moiré lattice wave vector and m_{ex} is the exciton effective mass. In the opposite limit, we expect resonances corresponding to exciton modes localized around the local minima of the moiré potential. In charge-neutral $MoSe_2/WS_2$ heterostructures, two bright moiré exciton resonances MX_1 and MX_2 are observed in the normalized reflection spectrum $\Delta R = (R - R_{bg})/R_{bg}$, where R and R_{bg} denote the reflection spectrum from the sample and background, respectively [see Fig. 1(c)]. The splitting between these two peaks of approximately 41 meV is significantly larger than the expected umklapp

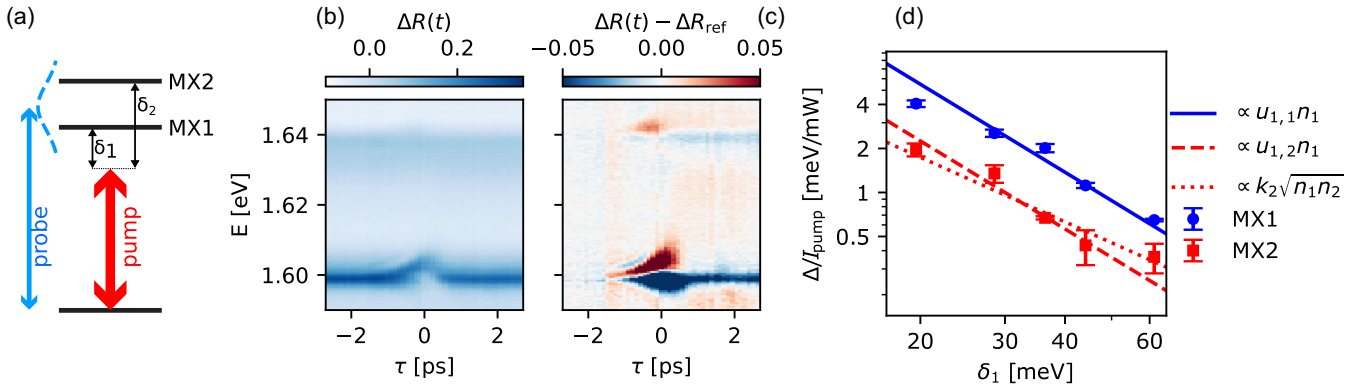

FIG. 2. Light shift of moiré excitons for cocircularly polarized pump and probe lasers. (a) Schematic of the moiré exciton energy level at charge neutrality. (b) Reflection spectrum as a function of the pump-probe delay, showing a clear blueshift of the lowest and brightest resonance MX_1 at zero time delay. The differential spectrum (c), obtained by subtracting from (b) a reference spectrum (acquired at $\tau < -2.5$ ps), reveals a blueshift of the upper and darker resonance MX_2 as well. (d) The dependence of the blueshift of MX_1 (blue circles) on the pump detuning scales as $1/\delta_1^2 \propto n_1$ (blue line) and stems from MX_1-MX_1 interactions. The shift of MX_2 (red squares) is well fitted either by a $\propto 1/\delta_1^2$ dependence (dashed red line) or by $\sqrt{n_1 n_2} \propto 1/(\delta_1\delta_2)$ (dotted red line). While we are not able to precisely deconvolve the role of these two potential contributions, both imply significant MX_1-MX_2 interaction and, hence, spatial overlap between these two bright moiré excitons.

splitting $(\hbar k_M)^2/(2m_{ex}) \approx 27$ meV for this system, which suggests that the moiré potential is strong enough to significantly alter the exciton spatial wave function within the moiré unit cell.

To reveal the elementary features of moiré excitons, such as their spatial extent and overlap, we investigate their mutual interactions using ac Stark spectroscopy. By measuring the light shift for co- and cross-circularly-polarized pump and probe beams, we probe interactions between moiré excitons in the same (cocircular) or opposite valley (cross-circular).

A. Cocircularly polarized light

Beginning with the scenario of cocircular polarization, we consider the evolution of ΔR as a function of the delay $\tau = t_{probe} - t_{pump}$, between the pump and probe pulse, as shown in Fig. 2(b) (here, the pump pulse is red-detuned from the MX_1 resonance by $\delta_1 = 20$ meV). The dominant coupling mechanisms between two same-valley excitons are electron and hole exchange interactions [43,44], which lead to short-range repulsion. Correspondingly, we observe a clear blueshift of the brightest exciton MX_1 for $|\tau| \lessapprox 0.2$ ps, that is, when the two pulses overlap in time (for more detail on the experimental setup, see Appendix A). To better assess the pump-induced modifications of weaker resonances, we use the differential reflection spectrum $\Delta R(t) - \Delta R_{ref}$, where ΔR_{ref} is a reference spectrum obtained when the probe pulse hits the sample significantly before the pump ($\tau \lessapprox -2.5$ ps): Figure 2(c) shows that a smaller blueshift of MX_2 is discernible in $\Delta R(t) - \Delta R_{ref}$. In a mean-field picture (detailed in Appendix H 4), the light shift Δ_i of MX_i ($i = 1, 2$) can be expressed as

$$\Delta_1 = 2u_{1,1}n_1 + 2u_{1,2}n_2 + 4k_1\sqrt{n_1 n_2}, \tag{1a}$$

$$\Delta_2 = 2u_{2,2}n_2 + 2u_{1,2}n_1 + 4k_2\sqrt{n_1 n_2}, \tag{1b}$$

where n_i is the density of MX_i excitons and we introduce four different interaction terms: $u_{i,j}$ correspond to exciton-exciton scattering conserving the moiré miniband populations, i.e., the processes $MX_i + MX_j \leftrightharpoons MX_i + MX_j$, while k_i correspond to processes where an exciton is scattered into a different moiré miniband, i.e., $MX_1 + MX_2 \leftrightharpoons MX_i + MX_i$. The density scales as $n_i \propto 1/\delta_i^2$ with the detuning δ_i of the pump from the MX_i resonance. Therefore, by tuning the pump laser frequency, one can change the density imbalance between the two excitons and, in principle, deconvolve the contribution of each scattering processes to the light shift. In practice, we observe signatures of an incoherent response for a blue-detuned pump, so we focus exclusively on red detunings. We consequently always have $\delta_1 < \delta_2$ and, thus, $n_1 > n_2$ [see Fig. 2(a)]. This imbalance is further amplified by the oscillator strength difference between MX_1 and MX_2.

Figure 2(d) shows the light shifts $\Delta_{1,2}$ as a function of δ_1 in a range where $n_1 \gtrsim 10n_2$. As a result, the light shift of MX_1 is dominated by MX_1-MX_1 interactions. From a fit, we obtain the interaction strength $u_{1,1}$, which we find to be larger by a factor $u_{1,1}/u_{ex} \approx 1.6 \pm 0.2$ than the moiré-free exciton-exciton interaction strength u_{ex}, measured on a monolayer $MoSe_2$ region of the same device. We tentatively attribute this enhancement to the reduced spatial extent of the MX_1 center-of-mass wave function within the moiré unit cell, which, in turn, increases the overlap between MX_1 excitons for a given average density.

Remarkably and despite the large imbalance $n_2 \ll n_1$, we observe a substantial light shift of MX_2, strongly increasing as the pump wavelength approaches the MX_1 resonance. This shift Δ_2 is not well reproduced by a $1/\delta_2^2$ dependence and attests to substantial interspecies interactions. A fit to our data does not enable us to precisely disentangle the respective contributions of the $MX_2 + MX_1 \leftrightharpoons MX_2 + MX_1$ and $MX_2 + MX_1 \leftrightharpoons 2MX_1$ processes. Nevertheless, we estimate that $0.3 \lesssim u_{1,2}/u_{1,1} \lesssim 0.8$, while we are not able to reliably estimate the k_i parameters (see Appendix C for more details on the fitting procedure).

These observations suggest a significant spatial overlap of MX_1 and MX_2 excitons and invalidates a simplistic picture of moiré exciton modes that are tightly confined around different high-symmetry points of the moiré potential. Moreover, our experiments are in reasonable qualitative agreement with the findings of moiré exciton wave functions obtained for the same structure using the continuum model [45]. In particular, we find that the latter predicts $u_{1,1}/u_{\mathrm{ex}} = 2.2$ and $u_{1,2}/u_{1,1} = 0.6$ (see Appendix H for details).

We point out that Eqs. (1a) and (1b) can be understood as arising from first-order perturbation theory. This approach is valid in the limit of sufficiently small pump power and large pump detuning. We find an empirical confirmation that we are indeed working in that regime by observing a linear dependence of the light shifts Δ_i with the pump intensity (Appendix B). Nevertheless, we can envision interesting higher-order effects arising from the mixing of the excitonic states. In particular, mixing of optically bright and dark excitons could be observed as the emergence of new resonances in the reflection spectrum.

B. Cross-circularly-polarized light

Since electron and hole exchange interactions are suppressed for excitons generated in opposite valleys, one may naively assume that the cross-circularly-polarized scenario should yield a significantly smaller light shift. However, the bare interaction of opposite valley excitons is attractive and supports a bound biexciton state, which has significant implications.

In order to illustrate how the biexciton state affects the exciton-exciton interactions, we briefly review the simpler scenario in which there is no moiré potential (such as in the case of monolayer TMDs). In this case, it is known that the presence of the biexciton resonance leads to an additional contribution to the light shift, scaling linearly with the inverse of the two-photon detuning $\delta_{\mathrm{b}}^{-1} = (-E_{\mathrm{b}} + \delta_{\mathrm{ex}})^{-1}$, where δ_{ex} is the detuning of the pump from the exciton resonance, E_{b} is the biexciton binding energy, and the probe is assumed resonant with the exciton. A hallmark of the biexciton is the ac Stark effect, where the light shift changes sign for detunings in the vicinity of E_{b} [36–40]. The two-photon resonance condition $\delta_{\mathrm{b}} = 0$ can be considered as a biexciton Feshbach resonance where the effective interactions between the pump- and probe-generated excitons change from being attractive ($\delta_{\mathrm{b}} > 0$) to repulsive ($\delta_{\mathrm{b}} < 0$).

We now extend these concepts to study the nature of biexcitons in moiré materials by measuring the ac Stark effect of MX_1 and MX_2 excitons under cross-circularly-polarized pump-probe lasers as a function of δ_1. We first observe that the sign of the ac Stark shift changes from a blueshift at small detunings [$\delta_1 \approx 22$ meV; Figs. 3(a) and 3(b)] to a redshift at large detunings [$\delta_1 \approx 45$ meV; Figs. 3(c) and 3(d)] for both moiré excitons. The full detuning dependence in Fig. 3(e) reveals that the sign change occurs at different detunings for MX_1 and MX_2 and is associated with two different *zero-quasimomentum* biexcitons. By contrast, a monolayer hosts only a single *zero-momentum* exciton. From a heuristic fit with the function $\Delta_i = a\tan^{-1}(\delta_1 - E_{\mathrm{b},i}/b) + c$ (with $i = 1, 2$ and a, b, c fitting parameters), we extract the binding energies $E_{\mathrm{b},1}$ and $E_{\mathrm{b},2}$ of the biexcitonic states determining the ac Stark shifts of MX_1 and MX_2, respectively. From the MX_1 light shift, we find $E_{\mathrm{b},1} \approx 36$ meV, which suggests that the ground state moiré biexciton (MX_1-MX_1) is more strongly bound here compared to a monolayer $MoSe_2$, where E_{b} was measured to be approximately 20 meV [36,38] or approximately 29 meV [34,46] (these variations could stem from different device architectures and dielectric environments). The light shift of MX_2 is related to a second biexciton state, with a mixed MX_1/MX_2 character and a binding energy $E_{\mathrm{b},2} \approx 28$ meV measured with respect to an unbound MX_1 and MX_2 exciton. Importantly, $E_{\mathrm{b},2}$ is smaller than the energy splitting between MX_1 and MX_2 (approximately 40 meV), and this second biexciton is higher in energy than two unbound MX_1 excitons. This should be contrasted with the monolayer scenario, where the bound state by definition has lower energy than two unbound zero-momentum excitons.

We further investigate the biexciton states of moiré excitons by modeling their scattering interactions in a periodic potential (see details in Appendix H). Our model incorporates short-range interactions calibrated to match the biexciton binding energy: We use the lower estimate $E_{\mathrm{b}} \approx 20$ meV [36,38] to account for screening effects from the proximal WS_2. Using parameters derived from density functional theory (Appendix H), we identify the bright excitonic resonances observed in experiment, which we show in Fig. 3(g). Here, we also show the bound biexcitons, which emerge due to spatial overlap of exciton wave functions within the moiré lattice.

The biexciton spectrum reveals that higher-energy biexcitons form in gaps within the two-exciton continuum, consistent with experimental observations. Specifically, the bound MX_1-MX_2 biexciton is enabled by significant spatial overlap between the exciton wave functions, with MX_2

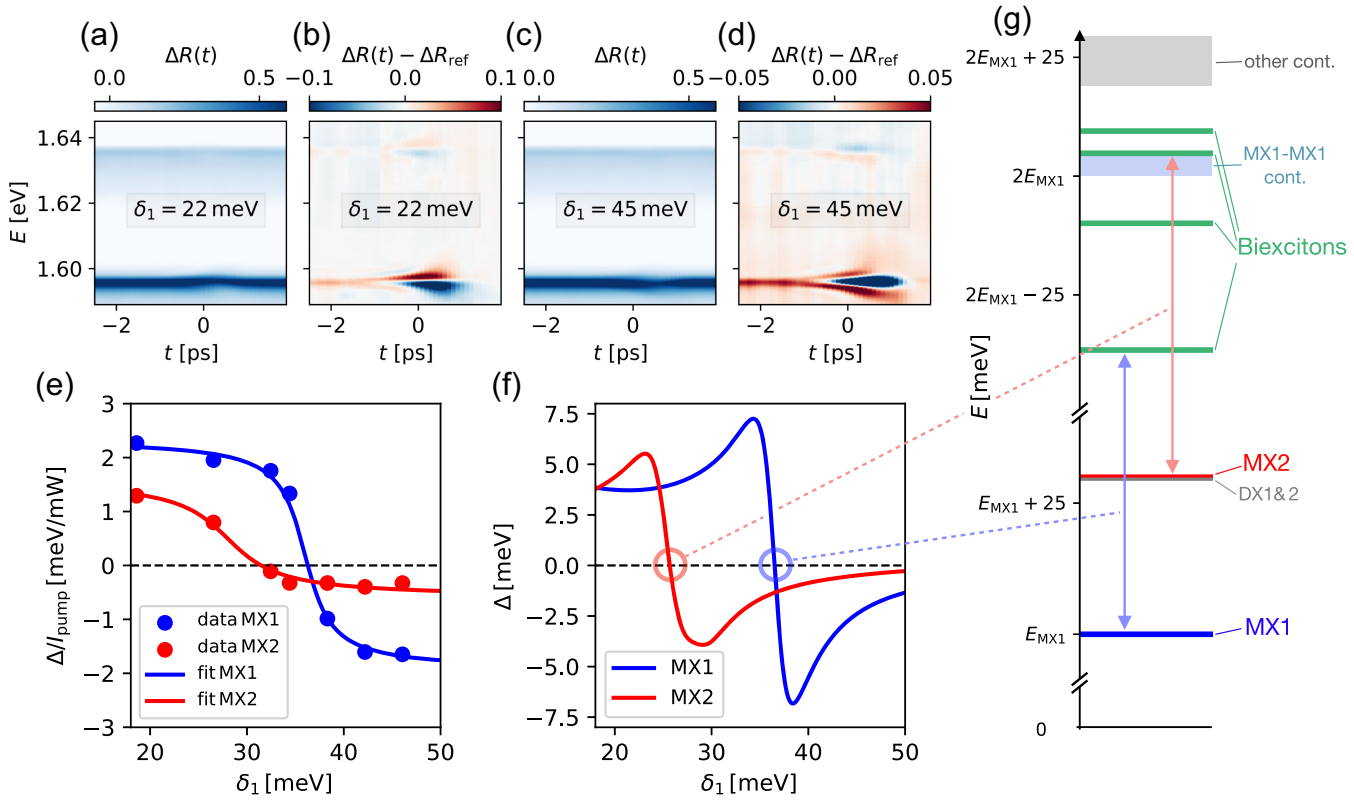

FIG. 3. Coupling to biexcitonic states. (a) Reflection spectrum as a function of the pump-probe delay when the pump is red-detuned by 22 meV from MX_1 and the pump and probe laser are cross-circularly polarized. (b) The differential spectrum, obtained by subtracting from (a) a reference spectrum (acquired at $t < -2.5$ ps), reveals a blueshift of both resonances MX_1 and MX_2. (c)(,d) A similar measurement carried out for a detuning of 45 meV from MX_1 shows instead a redshift of both resonances. (e) The dependence of the light shifts of MX_1 (blue dots) and MX_2 (red dots) displays a sign change for a pump detuning $\delta_1 \approx 36$ meV and $\delta_1 \approx 28$ meV, respectively. (f) The corresponding theory simulation for the light shifts of MX_1 (blue) and MX_2 (red) based on DFT moiré parameters. (g) The calculated spectrum which is shown in three different energy sectors with zero (defined as zero energy), one, and two excitons. In the one-exciton sector, there are the optically bright MX_1 and MX_2 excitons. In the two-exciton sector (focusing on zero center-of-mass quasimomentum), there exists a band of MX_1-MX_1 excitons (light blue) as well as other bands (gray) and bound biexcitons (green lines). We find that the sign change in the light shift of MX_1 and MX_2 in (f) can be attributed to the blue and red arrows (indicating exciton-biexciton transitions), respectively.

being notably more delocalized. The pump laser energies for exciting MX_1-MX_1 and MX_1-MX_2 biexcitons are highlighted in Fig. 3(g).

To connect theory with experiment, we calculate the exciton energy shifts induced by the pump laser (see Appendix H2 and H3). Here, we estimate the light-matter coupling strength such that the induced exciton density is on the order of 10^{11} cm^{-2} (see Appendix H3). The shifts are shown in Fig. 3(f) and agree qualitatively with measurements. The model suggests that only two biexcitons significantly influence the MX_1 and MX_2 shifts for the measured experimental detunings; the other biexcitons have negligible overlap with these two excitonic resonances. These results highlight how the emergence of interspecies biexcitons in moiré show clear and direct signatures in ac Stark spectroscopy.

III. ATTRACTIVE POLARON LIGHT SHIFT

When the $MoSe_2/WS_2$ heterostructure is electron doped, we observe an AP resonance that is redshifted from the MX_1 by approximately 35 meV. The corresponding trion binding energy is about 50% larger than that observed in monolayer $MoSe_2$, suggesting that the electron Wannier orbitals, as well as the optically generated trions, are strongly localized around the minimum of the moiré potential. Furthermore, the AP oscillator strength follows the number of singly occupied moiré sites, increasing linearly until $\nu = 1$ and then decreasing linearly until $\nu = 2$ [Fig. 4(a)]. This observation shows that the AP formation is hindered at doubly occupied sites due to the existence of local electron singlets that Pauli block the formation of (localized) trions. However, linear spectroscopy cannot be used to identify features that distinguish

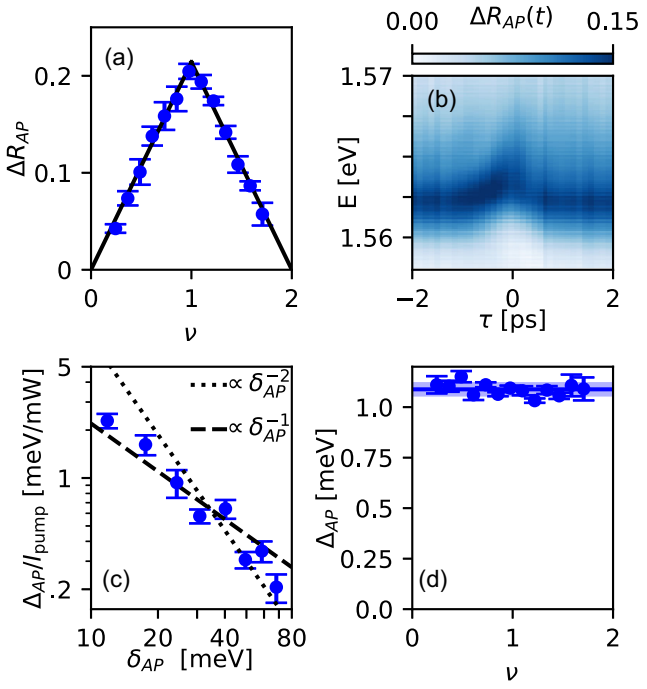

FIG. 4. Light shift of moiré polarons. (a) The peak reflection contrast as a function of gate voltage, showing that the oscillator strength of the AP linearly increases until $\nu = 1$ and then decreases linearly until $\nu = 2$. (b) Reflection spectrum $\Delta R_{\mathrm{AP}}(\tau)$ of the AP at $\nu = 1$ as a function of the pump-probe delay τ. (c) The observed AP blueshift is not driven by interactions as shown by its dependence on the pump detuning. (d) The measured light shift is remarkably constant as a function of ν, up to a small dispersion of approximately 3% (shown as a blue stripe) compatible with statistical fluctuations (shown as an error bar, obtained for each point by repeating the measurement four times). The combination of linear $1/\delta_{\mathrm{AP}}$ dependence of the light shift and its independence of ν demonstrate the lack of interactions between APs or trions localized on different moiré sites.

APs in deep moiré potentials from their counterparts in weak moiré potentials or in monolayer TMDs.

Figure 4(b) shows the pump-probe measurement as a function of τ for $\delta_{\mathrm{AP}} = 12$ meV, clearly showing a blueshift of the AP resonance with negligible alteration of the resonance for $\tau \geq 0.2$ ps. While this measurement is reminiscent of the result for MX_1, Fig. 4(c) shows a striking difference in the δ_{AP} dependence: The AP light shift is better fit using a $1/\delta_{\mathrm{AP}}$ dependence, typical of the ac Stark shift observed for an ensemble of noninteracting two-level emitters. We tentatively explain this observation by arguing that the AP resonance can be considered as stemming primarily from a collective excitation of trions localized at the M-M sites of the moiré lattice. In the absence of intersite hopping, the excitation of a trion at a given site cannot depend on the existence of a trion on any other site, ensuring that moiré trions behave as noninteracting excitations. The only contribution to the light shift in this limit comes from the ac Stark shift of each site independently, whose magnitude scales as $1/\delta_{\mathrm{AP}}$. Small but nonzero hybridization of the collective trion excitation with the bare exciton could give rise to a finite interaction strength, a finite intersite hopping due to long-range electron-hole exchange, and a deviation from the pure $1/\delta_{\mathrm{AP}}$ contribution to the light shift. We note that recent experiments on the same moiré structure yielded magnetization signatures consistent with unexpectedly weak intersite hopping [7].

We find the first confirmation of this explanation when we measure the electron density dependence of the light shift: Figure 4(d) shows that varying ν from 0 to 2 results in negligible variation in the magnitude of the light shift, despite large variation in the pump-induced virtual AP population. This behavior contrasts with the strong electron density dependence of the AP light shift previously observed in a monolayer $MoSe_2$ [34].

An additional confirmation of our description of the moiré AP as a collective excitation of noninteracting localized trions is provided by complementary measurements where we study the saturation behavior of the AP resonance under resonant pump-laser excitation. Figure 5(a) depicts a cartoon of the heterostructure where resonant excitation leads to localized trion occupation, which, in turn, Pauli blocks further excitation. To investigate the associated saturation of the AP resonance, we measure ΔR as a function of the electron density in cross-linear configuration for various pump laser intensities. Figure 5(b) shows that, for pump laser power $P_p = 40$ μW, the AP resonance blueshifts and weakens for short pump-probe time delays. Figure 5(c), in turn, shows that increasing P_p leads to saturation of ΔR for all electronic densities in the range $0 \leq \nu \leq 2$. This saturation behavior, characteristic of an ensemble of noninteracting two-level emitters, can be explained by arguing that each occupied moiré site is driven into a balanced mixture of its ground (single-electron) and excited (trion) states for $P_p \geq 50$ μW. In stark contrast, saturation of composite-boson excitations, such as itinerant excitons or APs, leads to a gradual loss of oscillator strength, accompanied by a shift of the resonance energy. Figure 5(e) shows that the saturation under cross-linear excitation with $P_p = 40$ μW is near complete for pump-probe time delay $\tau \lesssim \tau_{\mathrm{pump}}$, where the probe ΔR is reduced by a factor of $\simeq 2$, as compared to its reference value obtained without the pump laser. We remark that the relaxation time of approximately 5 ps of the resonantly excited APs observed in Fig. 5(e) is much longer than the pump pulse duration $\tau_{\mathrm{pump}} \simeq 0.1$ ps. This long-time dynamics is most likely due to the generation of a (real) trion population through absorption of resonant photons.

The aforementioned cross-linearly-polarized measurements ensure that both the pump and probe lasers drive trion formation on all moiré sites, regardless of the electron

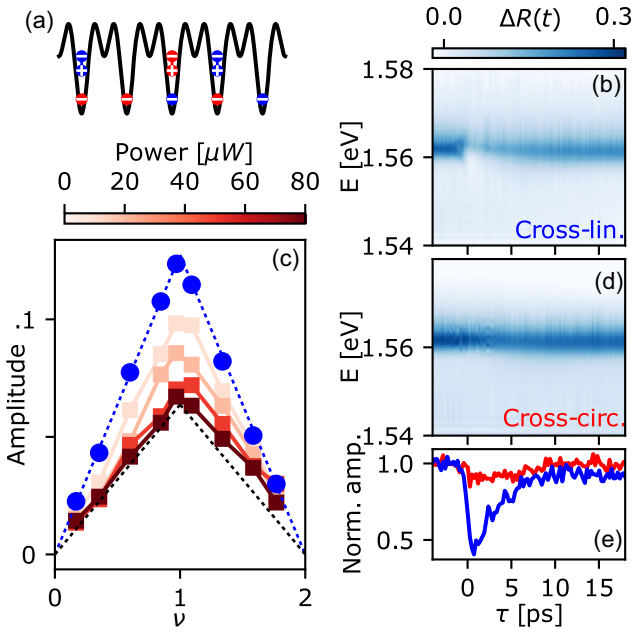

FIG. 5. Resonant excitation of moiré polarons. When the pump and probe lasers are cross-linearly polarized, they drive the AP transition at all moiré sites [see the sketch in (a)]. We observe a blueshift and a reduction of the AP reflection amplitude (b). The latter is plotted in (c) as a function of the electronic filling factor ν of the moiré lattice. The blue dots are obtained without pump and the red squares for various pump intensities. For a sufficiently large intensity, all sites end up in a statistical mixture of a single electron and a moiré trion, and, consequently, the amplitude of the AP resonance is divided by a factor of 2 (dashed black line). After the pump pulse is gone, the AP resonance recovers on a timescale of approximately 5 ps [(e), blue line]. In contrast, using cross-circularly-polarized lasers, the pump and the probe pulse are driving the AP transition on different moiré sites, and, consequently, we do not observe any effect of the pump [(d), (e), red line].

spin. We also perform a test experiment using a cross-circular configuration. In that case, the pump and the probe are addressing singly occupied sites with electrons in the opposite valley. Consequently, the probe reflection is unaffected by the pump [Figs. 5(d) and 5(e)]. This result stands in contrast to prior measurements on monolayer $MoSe_2$, where in cross-circular configuration we observe a redshift of the AP resonance, which we tentatively attribute to phase space filling induced by the virtual AP population generated by the pump pulse [34].

We conclude that the pump-induced light shift and bleaching of the AP transition demonstrates that the AP resonance can be described as an ensemble of noninteracting two-level emitters and, as such, is inconsistent with the exciton-polaron model that successfully describes the optical spectrum of monolayer TMDs [12–14] as well as APs in weak moiré potentials [47]. For electron densities satisfying moiré filling factor $\nu > 1$, another resonance emerges in the spectrum which we term MX_3 [Fig. 1(c)]. The ac Stark shift of MX_3 is similar to that of monolayer AP or exciton resonances, which allows us to tentatively identify it as excitons or APs generated at doubly occupied moiré sites. These measurements are detailed in Appendix F (see Fig. 10): Briefly, MX_3 displays a density-dependent ac Stark shift, contrasting with that of the AP discussed above, which we attribute to repulsive interactions. Interestingly, the light shift is smaller for integer fillings $\nu = 2$ and $\nu = 3$, where the oscillator strength is larger and where the electrons form incompressible states. This counterintuitive behavior is qualitatively understood from the enhancement of the interaction when the electron system is compressible and efficiently mediates interaction between exciton polarons [34,48].

IV. DISCUSSION

Our findings shed new light on the nature of moiré excitons and polarons, which remains a topic of active research [5,22–27,41,49–57]. In particular, we show how nonlinear spectroscopy unveils the itinerant or localized character of moiré optical excitations. Our experiments allow us to assess the extent of spatial overlap between different moiré excitons or attractive polarons. It is somewhat remarkable that this information is accessible to far-field optics given that the moiré length scale is about 2 orders of magnitude below the optical resolution. The insight we obtain is crucial for the interpretation of experiments aimed at optical sensing of correlated electronic states [4–8,16,17]. While the heterostructure we study exhibits a deep triangular moiré potential, favoring topologically trivial correlated electronic insulators and localized AP, we envision that applying ac Stark spectroscopy to twisted homobilayers exhibiting Chern bands could reveal features not accessible to linear spectroscopy. For example, we expect the AP ac Stark shift to change qualitatively as the system is tuned from a fractional Chern insulator quantum fluid to a Mott-Wigner state with strongly localized charges, using an applied displacement field [8,9]. We also expect the ac Stark shift of the AP resonance to reveal signatures of the quasigap to charged excitations of a composite Fermi liquid at half filling of a Chern band [58].

The experiments detailed in Fig. 5 present a realization of a nonequilibrium Bose-Fermi mixture consisting of electrons in a flat moiré band and optically injected excitons [18–21]. The choice of resonant excitation of the AP transition forces the mixture into a state that can be described as a high-density moiré trion gas. Using a circularly polarized resonant pump laser and an external magnetic field to valley polarize electrons, it may be possible to create a trion at each moiré site, thereby realizing a solid-state analog of the Dicke model [59].

The dressing of a quantum material with virtual optical excitations could be a promising route to engineer new phases of matter. The idea of using an intense laser pulse to modify material properties has already been demonstrated [60], but it often suffers from incoherent pumping and heating effects when an electronic polarization mode of the system is resonantly driven. Similar, albeit much less severe, problems in driven atomic systems can be alleviated using Rydberg dressing, where an off-resonant laser effects coherent hybridization of a ground (or long-lived low-energy) state and a Rydberg state: The atoms remain mostly in the ground state and spontaneous emission is strongly suppressed, but virtual excitations to the Rydberg state still ensure long-range interactions. Similarly, it was proposed that virtual excitons in bulk semiconductors could mediate ferromagnetic interactions between free electrons in the bulk [61] or trapped in quantum dots [62]. Our experiments demonstrate that an intense pump laser can realize an efficient excitonic dressing of a moiré system while keeping light absorption negligible thanks to a large detuning from the resonances. This approach could provide a new path toward light-induced magnetism in van der Waals heterostructures [63].

ACKNOWLEDGMENTS

We thank A. Christianen, M. Glazov, M. Hafezi, A. Müller, A. G. Salvador, R. Schmidt, and A. Srivastava for inspiring discussions. This work was supported by the Swiss National Science Foundation (SNSF) under Grant No. 200020_207520. B. E. acknowledges funding from an ETH postdoc fellowship. H. S. A. acknowledges support from the Swiss Government Excellence Scholarship. T. U. acknowledges support from the Funai Overseas Scholarship.

DATA AVAILABILITY

The data are available at the ETH Research Collection [64].

APPENDIX A: EXPERIMENTAL SETUP AND SAMPLE FABRICATION

The sample is measured in a dry cryostat (Attodry800, Attocube) at cryogenic temperatures of approximately 5 K with free-space optical access and equipped with nanopositioners allowing displacement along the three axes. For the pump and probe, we use a mode-locked Ti:sapphire laser (Tsunami, Spectra-Physics), with a repetition rate of 76 MHz and pulse duration of approximately 100 fs. The pulse is split along two paths for the pump and the probe. The bandwidth of the pump is reduced using a pulse shaper, and its power is controlled using a motorized optical attenuator. We achieve a larger spectral width for the probe using a nonlinear fiber (femtowhite 800, NKT Photonics) which produces a quasicontinuum around the investigated resonances. The length of the probe optical path can be varied using a retroreflector on a motorized translation stage, enabling a fine-tuning of the time delay between the two pulses. Both beams are focused on a diffraction-limited spot on the sample using an apochromatic microscope objective with NA = 0.8 (LT-APO/VISIR/0.82, Attocube). The typical probe power is on the order of a few microwatts. The reflected light spectra are recorded using a Peltier-cooled CCD camera.

For the sample fabrication, few-layer graphite, approximately 35 nm *h*-BN, monolayer $MoSe_2$ and WS_2 are mechanically exfoliated. The layers are assembled using the dry-transfer technique with a poly(bisphenol A carbonate) film on a polydimethylsiloxane (PDMS) stamp and deposited on a 285 nm Si/SiO_2 substrate [65]. The crystal alignment of the TMDs is determined prior to the stacking measuring the generation of second-harmonic light as a function of the polarization of an incoming infrared laser pulse. They are then stacked with a negligible twist. The graphene top and bottom gates and TMDs are contacted using gold electrodes deposited using optical lithography and electron beam deposition.

APPENDIX B: DATA ANALYSIS

In order to extract the light shift amplitude, we first fit the reflection spectrum for various time delays and extract the resonance position(s). The result is shown in Fig. 6(a) in the case of the MX_1 resonance. We then perform a Gaussian fit of the measured line shift as a function of the pump-probe delay in order to extract the light shift amplitude at zero time delay. To determine the dependence of the light shift on the pump detuning, we perform for each pump wavelength a measurement at various pump powers as shown in Fig. 6(b). In this way, we can use relatively low power for a near-resonant excitation and larger power at larger detunings, always making sure that we are in a regime of linear scaling with power. In the figures in the main text, we plot the slope Δ/I_{pump} computed from a linear fit at each pump detuning δ.

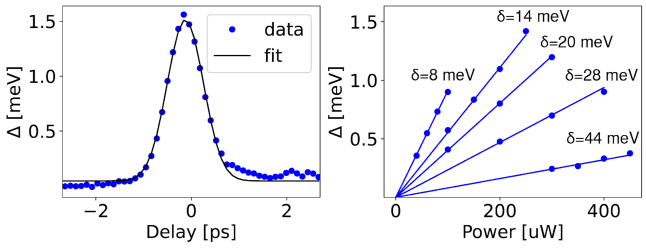

FIG. 6. Data analysis. (a) Light shift as a function of the pump-probe delay for MX_1 for a pump power of 250 μW and detuning of 11 meV, showing a clear blueshift at zero time delay. The fit corresponds to a Gaussian envelope. (b) The dependence of the light shift of MX_1 on pump power at different pump detunings δ_1 exhibits a linear dependence.

APPENDIX C: FIT OF THE WAVELENGTH DEPENDENCE

We discuss here our analysis of the wavelength dependance of the light shift. Taking into account a single resonance, the light shift Δ can be expanded in a series of $1/\delta$ using perturbation theory [30]. The first-order $1/\delta$ term comes from light-matter interaction, while exciton-exciton interactions contribute to higher-order terms, in $1/\delta^2$ or $1/(\delta_i\delta_j)$ when several modes contribute. In principle, a fine analysis of the detuning dependence of the light shift would enable one to deconvolve the various contributions. In practice, this analysis can be challenging due to the finite range of detuning in which we can take reliable data. Indeed, for all resonances, we had to restrict the data to a window of approximately [20, 80] meV. Going closer to resonance, we face two issues: First, incoherent effects become more prominent as pump photons carry enough energy to generate a real population of excitons and, hence, are more likely to be absorbed. Second, the perturbative expansion of the light shift becomes inconsistent when $\Delta \sim \delta$. Conversely, going further away from resonance the signal reduces (given the available laser power) and the extraction of the light shift becomes unreliable. Furthermore, in that regime, the light-matter terms $\propto 1/\delta$ become stronger compared to the interaction term $\propto 1/\delta^2$ that we are interested in.

1. Charge neutrality

With the relatively small detuning we use (compared to the exciton Rydberg energy), the exciton-exciton interaction is expected to be the dominant contribution to the light shift [34]. This is indeed confirmed by our data, which are not compatible with a $1/\delta$ law. Let us, thus, focus on the interaction-induced light shift, which we generalize to our moiré system with two bright exciton modes. As shown in Appendix H 4, the light shifts of MX_1 and MX_2 read, respectively,

$$\Delta_1 = 2u_{1,1}n_1 + 2u_{1,2}n_2 + 4k_1\sqrt{n_1 n_2}, \tag{C1}$$

$$\Delta_2 = 2u_{2,2}n_2 + 2u_{1,2}n_1 + 4k_2\sqrt{n_1 n_2}, \tag{C2}$$

with the densities scaling as $n_i \propto |\Omega_i\phi_i(0)|^2/\delta_i^2$. The ratio $r = |\Omega_1\phi_1(0)|^2/|\Omega_2\phi_2(0)|^2 = \gamma_{\mathrm{rad},1}/\gamma_{\mathrm{rad},2} \approx 0.48$ can be obtained from a fit of the reflection contrast (see Appendix D). Using this independent estimate and performing a joint fit of $\Delta_{1,2}$, we reduce the number of fitting parameters to five: A, $u'_{2,2}$, $u'_{1,2}$, k'_1, and k'_2, where $u'_{i,j} = u_{ij}/u_{1,1}$, $k'_1 = k_i/u_{1,1}$, and

$$\Delta_1 = A\left(\frac{1}{\delta_1^2} + \frac{r^2 u'_{1,2}}{\delta_2^2} + \frac{2rk'_1}{\delta_1\delta_2}\right), \tag{C3}$$

$$\Delta_2 = A\left(\frac{r^2 u'_{2,2}}{\delta_2^2} + \frac{u'_{1,2}}{\delta_1^2} + \frac{2rk'^{2,2}_2}{\delta_1\delta_2}\right). \tag{C4}$$

Furthermore, within a Born approximation $u_{ij}^{kl} \propto \int dr\phi_i\phi_j\phi_k^*\phi_l^*$ (see Appendix H 4) and using the Cauchy-Schwarz inequality, we obtain the following bounds: $0 < u'_{1,2} < [u'_{2,2}]^{1/2}$, $|k'_1| < [u_{1,2}]^{1/2}$, and $|k_2{}'| < [u'_{2,2}u'_{1,2}]^{1/2}$, which we enforce to improve the convergence of the fit.

For MX_1 [see Fig. 7(a)], the full fit reveals the dominant contribution to be the MX_1-MX_1 interaction. We obtain the fitting parameter A, which we can compare to the value obtain from fitting the light shift of a monolayer exciton (on

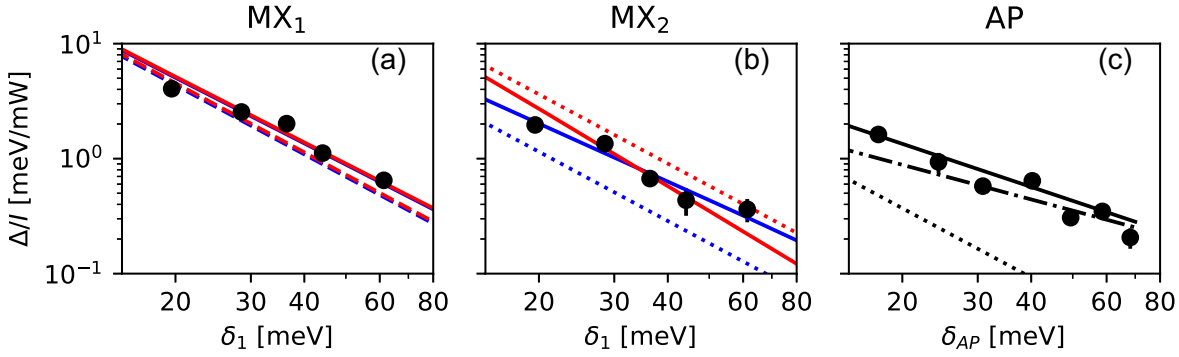

FIG. 7. Pump wavelength dependence. From a fit, we infer the origin of the light shift of MX_1 (a), MX_2 exciton (b), and the attractive polaron at $\nu = 1$ (c). At charge neutrality [(a),(b)], we are not able to deconvolve the contribution of the $u'_{1,2}$ and k'_2 fitting parameters [see Eq. (C4)]. We, thus, perform two fits, setting k'_2 to its upper and lower bounds, shown as a solid blue and red line, respectively. For the MX_1 exciton (a), the light shift is dominated by the $2u_{1,1}n_1$ term (shown as a dashed line) and barely sensitive to the MX_2-dependent terms, so both fits are nearly identical and we obtain a good estimate of $u_{1,1}$. For MX_2 (b), both fits are in fair agreement with the data, but the contribution of the $2u_{1,2}n_1$ term (dotted line) is significantly different, and we are, thus, able to provide only a rather broad confidence interval for $u_{1,2}$. For the AP, a fit $A_{\mathrm{AP}}/\delta_1 + B_{\mathrm{AP}}/\delta_{\mathrm{AP}}^2$ [solid black line, (c)] suggests that the usual ac Stark shift scaling as A_{AP}/δ_1 (dash-dotted line) is occurring instead of an interaction-driven shift scaling as $B_{\mathrm{AP}}/\delta_{\mathrm{AP}}^2$ (dotted line).

a monolayer $MoSe_2$ region of the same device). We estimate $u_{1,1}/u_{ex} \approx 1.6 \pm 0.2$, where u_{ex} is the monolayer exciton-exciton interaction (see Appendix E for an absolute calibration).

For MX_2 [see Fig. 7(b)], the fit is unable to reliably disentangle the contribution of the second and third terms of Eq. (C4), corresponding to the scattering of an MX_1 exciton, without (first term) or with (second term) a change of moiré band. Indeed, performing a fit with each of these two terms independently, we obtain in both cases a reasonable agreement with the data over the full detuning range. We thus perform two fits, where the coupling $k_2' = \pm[u_{2,2}' u_{1,2}']^{1/2}$ saturates the Cauchy-Schwarz inequality. In this way, we obtain the bounds $0.3 \lessapprox u_{2,2} \lessapprox 0.8$.

2. Moiré attractive polaron

For the AP [Fig. 7(c)], the light shift is typically smaller and more noisy due to the weakness of the transition. As a result, it is more difficult to discriminate a potential $1/\delta$ and $1/\delta^2$ dependence. Nevertheless, the fit does suggest that the former is here the leading contribution, consistent with the picture of an ensemble of distinguishable and noninteracting two-level systems, as argued in the main text.

APPENDIX D: TRANSFER MATRIX SIMULATION

In order to infer the interaction strength of the various moiré excitons from their light shift, we need to estimate the exciton density that we generate and, hence, the exciton oscillator strength. The latter can be obtained from a fit of the reflection spectrum. Such a fit needs to include the reflection of the electromagnetic field on the interfaces between the various dielectrics that make our van der Waals heterostructure. We do this using the transfer matrix method [66]. Two fitting parameters for the background are the *h*-BN thickness of approximately 31 nm and approximately 37 nm for the top and bottom layer, respectively, and the *h*-BN refractive index $n_{h\text{-BN}} \approx 2.15$ [67,68]. Then, for each resonance, we have three additional fitting parameters, namely, its energy and radiative and nonradiative decay rates. The results of this fit are shown in Fig. 8. We show here the bare reflection spectrum, obtained using a light source that is to a very good approximation spectrally flat in the energy range shown in the figure. We are unable to obtain a perfect fit of the background, using the *h*-BN thicknesses and refractive index as free parameters. The discrepancy that we observe, especially on the edge of the spectrum, could be due to chromatic aberrations (although we are using a microscope apochromatic objective to limit those). Nevertheless, in the center of the spectrum, we are able to reproduce our spectra very well at all fillings.

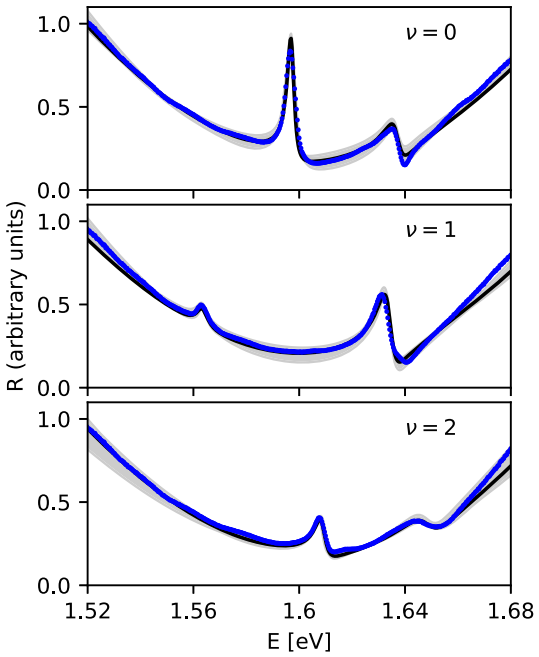

Resonance	ν	$\hbar\gamma_{rad}$ [meV]	$\hbar\gamma_{non\text{-}rad}$ [meV]
MX_1	0	1.0 ± 0.2	1.3 ± 0.3
MX_2	0	0.48 ± 0.1	2.8 ± 0.4
AP	1	0.27 ± 0.1	2.7 ± 0.4
MX_2'	1	1.1 ± 0.3	2.9 ± 0.4
MX_3	2	0.52 ± 0.1	2.2 ± 0.3

FIG. 8. Fit of the reflection spectrum using transfer matrix simulation. The blue dots are the data, and the black solid line is a fit (gray area span by varying the fitting parameters within the confidence interval).

APPENDIX E: INTERACTION STRENGTH

The radiative (γ_r) and nonradiative (γ_{nr}) decay rates can be used to extract the density of excitons n_{ex} induced by the pump. Using the optical Bloch equations within the adiabatic approximation, we have [66]

$$n_{ex} = \frac{2I_i\gamma_r}{(\gamma_r + \gamma_{nr})^2 + \delta_{ex}^2}, \tag{E1}$$

where I_i is the photon flux. For reference, we first look at the exciton light shift Δ_{ex} measured on a monolayer region of the sample, as a function of the exciton density; see Fig. 9. We observe a linear dependence $\Delta_{ex} = u_{ex} n_{ex}$, from which we extract the exciton-exciton interaction strength $u_{ex} \approx 0.06(3)\ \mu\text{eV}\,\mu\text{m}^2$. The latter is compatible with previous measurements [34,48,66,69], although significantly smaller than theoretical estimates, $\sim 3E_{ex}a_{ex}^2 \sim 1\ \mu\text{eV}\,\mu\text{m}^2$, where E_{ex} is the exciton binding energy and a_{ex} is the exciton Bohr radius [43,44].

From the measurement of the light shift of the moiré excitons and polaron shown in Fig. 7, we obtain $u_{1,1} \approx 1.6u_{ex}$ and $u_{1,2} \approx 0.7u_{ex}$ and, for the MX_3-MX_3 interaction, $u_{3,3} \approx 5.3u_{ex}$. The enhancement of the interaction strength

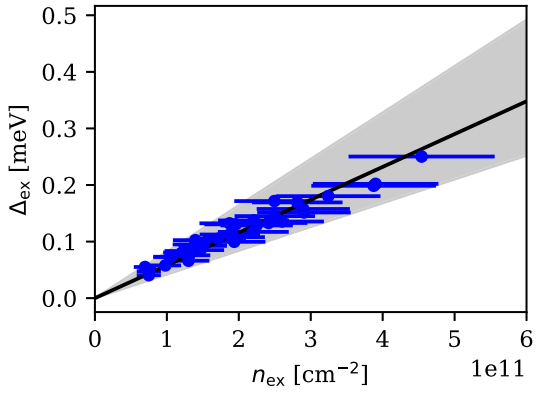

FIG. 9. Light shift as a function of the exciton density. The blue dots are the data, obtained for various powers and detunings. The error bars come from the uncertainty of the exciton decay rates and on the power on the sample. The black solid line is a fit with the gray area span obtained by varying the fitting parameters within the confidence interval.

of MX_1 (charge neutrality) could stem from the partial confinement induced by the moiré potential. The larger enhancement for MX_3 reflects the polaronic nature of this resonance, as previously observed in a monolayer sample [34].

APPENDIX F: LIGHT SHIFT OF MX_3 IN THE REGIME OF LARGE DOPING

Even though MX_3 is the dominant excitonic resonance for electron filling factors $\nu \geq 1.5$, its identification has remained unclear. To gain insight, we investigate the nonlinear response of the MX_3 resonance. Figures 10(a) and 10(b) show the reflection amplitude and the energy of MX_3 for $1.5 \leq \nu \leq 3.4$ in the absence of a pump laser: Consistent with earlier observations, we find that the resonance energy as well as the reflection strength, or, equivalently, the oscillator strength, of MX_3 exhibit local maxima at integer fillings $\nu = 2$ and $\nu = 3$. These features could be explained by partial suppression of dynamical dressing of excitons by electrons, when the two-dimensional electron system (2DES) is in an incompressible state [16,70]. In contrast, when the electrons form a Fermi liquid ($\nu \neq 2, 3$), the dynamical dressing of MX_3 is more effective and results in a redshift together with a reduction of the oscillator strength.

Figure 10(c) shows the light shift as a function of pump-probe delay τ for four representative filling factors obtained for $\delta_3 = 80$ meV. We observe that the light shift for $\tau \simeq 0$ indicates repulsive (attractive) interactions between same (opposite) -valley MX_3 excitons generated by co- (cross-) circularly polarized pump-probe fields. While attractive interactions between opposite-valley excitons have been reported before, it is surprising that the magnitude of the light shift is comparable in the two cases. The attractive interactions for the cross-polarized configuration may be explained through a near-resonant two-photon (pump + probe) excitation of the biexciton resonance at ω_{XX}. Verification of this hypothesis could be achieved by changing the pump detuning δ_3 so as to probe both $\delta_3 \leq \omega_{XX}$ and $\delta_3 \geq \omega_{XX}$, since, for the latter case, the biexciton-mediated interactions would become repulsive. As we had to choose $\delta_3 < \omega_{XX}$ to avoid strong background absorption, we could not verify the role of biexciton in the measured light shift.

In contrast to the light shift measurements in the charge-neutral regime, we find that the pump pulse results in a MX_3 line shift that increases linearly with τ for $0.2 \leq t \leq 3.0$ ps. Moreover, the linear shift at a given ν is identical for co- and cross-circularly-polarized pump-probe configurations but has a different sign for compressible ($\nu \neq 2, 3$) and

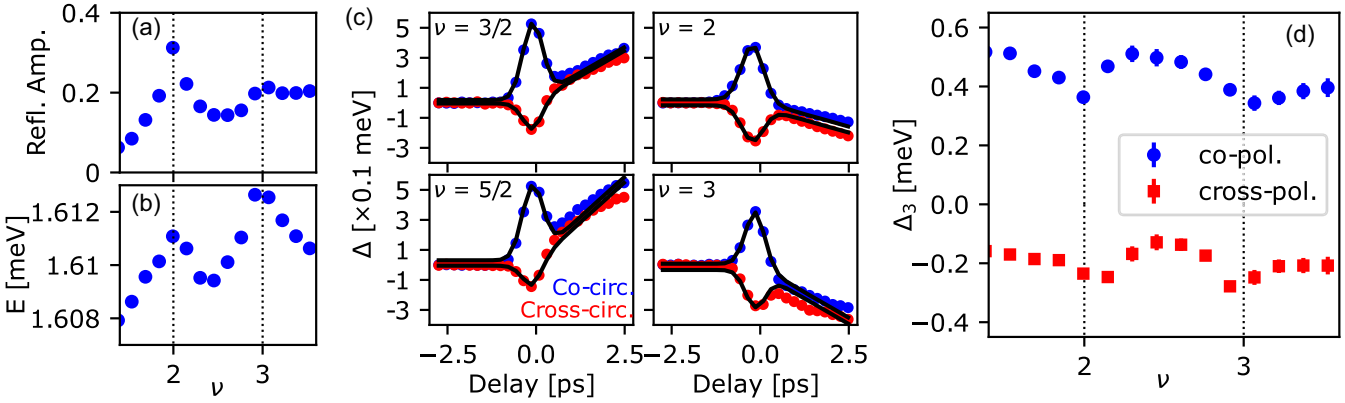

FIG. 10. Light shift of MX_3. The resonance MX_3 shows distinctive kinks in its amplitude (a) and energy (b) at integer fillings of the moiré lattice with electrons, following the changes in the 2DES compressibility. The light shift of the moiré exciton MX_3 at various fillings (c) is well fitted by a line on top of a Gaussian function (black line). The latter captures the coherent response of the system, which corresponds to an interaction-induced blueshift for cocircularly polarized pump and probe and possibly to a redshift stemming from the coupling to the biexciton states in a cross-circular configuration. The amplitudes of these two shifts are sensitive to the polaron dressing of the exciton and, consequently, are extremal at integer filling of the moiré lattice (d).

incompressible ($\nu = 2, 3$) electron states. We tentatively explain this feature by generation of free carriers by nonresonant absorption of pump photons that change the electron density for timescales well exceeding the pump duration.

Since the MX_3 resonance energy has maxima (minima) for $\nu = 2, 3$ ($\nu = 3/2, 5/2$), any pump-induced change in electron density will result in a redshift (blueshift) of the resonance energy. While we do not understand why the redshift (blueshift) depends linearly on τ for $\tau > \tau_{\text{pump}}$, we speculate that pump-induced charges are initially generated in high-energy bands and that they influence the nonlinear response only as they relax to the lowest-energy available moiré band.

We also observe in Fig. 10(c) that the magnitude of the light shift for the cocircularly polarized pump-probe configuration is smaller for incompressible states. Plotting Δ_3 as a function of ν [Fig. 10(d)] shows that the blueshift is indeed minimal for $\nu = 2, 3$. This is at first glance surprising, given that the oscillator strength, and, consequently, the generated MX_3 population, is maximal for these incompressible states. However, it was recently shown that interactions between attractive exciton polarons [34,48,71] mediated by their dressing cloud are dramatically enhanced compared to those of bare excitons. Such an enhancement of interaction strength may overcome the reduction of the oscillator strength of MX_3 for $\nu \neq 2, 3$. This tentative explanation suggests that the MX_3 mode may be identified as a second attractive polaron mode where the exciton is dressed by electrons in the upper moiré band. Last but not least, we find that the redshift of MX_3 in the cross-circularly-polarized configuration is maximal when the electronic state is incompressible; we currently do not have an explanation for this observation.

APPENDIX G: LIGHT SHIFT OF MX_2' AT $\nu = 1$

At a unity filling $\nu = 1$ of the moiré potential, we observe two bright resonances, the AP which we discuss in detail in the main text, and MX_1', emerging from MX_2 and which we now investigate. Depending on the pump and probe polarizations, we observe different behaviors. In cocircular polarization, we obtain the usual blueshift which we attribute to MX_2'-MX_2' interactions. Contrary to other resonances, we cannot confirm this claim by an analysis of the detuning dependence. Indeed, we observe strong incoherent behavior for a pump blue detuned from the AP, and we, therefore, explore only the red-detuned situation. Specifically, we explore the range $\delta_{MX2'} \approx [80, 110]$ meV in which we observe no significant evolution of the light shift, as expected from a scaling as $1/\delta^2_{MX_2'}$; see Fig. 11(a). By contrast, in cross-circular polarization, we observe a distinct redshift which diverges close to the AP resonance, in excellent agreement with a $1/\delta^2_{AP}$ scaling and suggesting an attractive interaction between AP and

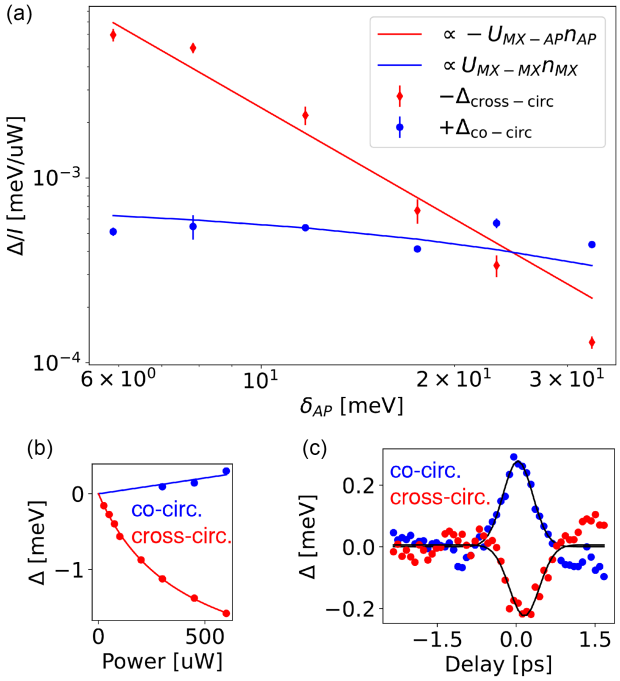

FIG. 11. Light shift of MX_2' at $\nu = 1$. (a) Detuning dependence of the light shift of the resonance MX_2' at a filling $\nu = 1$. Red dots correspond to cross-polarized pump and probe and show a redshift of the MX_2' resonance which can be well fitted (red line) by a dependence $\propto 1/\delta^2_{AP}$ stemming from MX_2'-AP interactions. Blue dots correspond to copolarized pump and probe and show a blueshift of the MX_2' resonance which can be well fitted (blue line) assuming MX_2'-MX_2' interactions and a scaling $\propto 1/\delta^2_{MX_2'}$. (b) Light shift of MX_2' as a function of pump power in different polarizations. Cross-circular polarization shows a distinct redshift; the deviation from a linear dependence is due to saturation of the AP population at large powers. Collinear polarization shows a smaller blueshift which is well in the linear regime. (c) MX_2' shift vs pump-probe time delay in cocircular (blue) for a pump power of 500 μW and cross-circular (red) polarizations for 50 μW.

MX_2' in opposite valleys. We point out that a similar behavior was observed in a monolayer system and tentatively attributed to the reduction of the phase-space filling upon the generation of an AP, for an opposite-valley exciton [34]. The pump power dependence [Fig. 11(b)] of the light shift shows an interesting behavior for a near-resonant excitation of the AP $\delta_{AP} \approx 8$ meV. In that case, at high intensity, we expect a saturation of the AP density as the moiré potential is filled up, as described in the main text (although here, keeping a finite δ_{AP}, we are unable to fully saturate the transition). Indeed, we observe a sublinear increase of the cross-polarized light shift attributed to AP-MX_2' interactions. On the contrary, the copolarized light shift which we attribute to MX_2'-MX_2' interactions is linear in the pump power, as the density of MX_2' remains far from saturation of the moiré lattice ($\delta_{MX_2'} \approx 80$ meV).

APPENDIX H: THEORETICAL MODEL

In this section, we primarily provide a detailed description of the theoretical model used to analyze the charge-neutral, cross-circular polarization data. The foremost goal of this model is to qualitatively capture the energy shifts observed in the MX_1 and MX_2 exciton resonances when subjected to the influence of a pump laser. To this end, we calculate the exciton-exciton T matrix in the presence of a moiré potential, which is inspired by a recent treatment of two interacting atoms in a 2D square optical lattice [72]. This approach allows us to capture the essential physics of the interaction under the influence of the pump.

We conclude the section with a brief discussion on a model for the cocircular polarization data. For ease of notation, we set $\hbar = 1$.

1. Model for interactions of two distinguishable excitons

We begin by modeling the interactions between two distinguishable rigid ($1s$) excitons in the presence of moiré. The Hamiltonian we consider consists of four terms:

$$H = H_{X\uparrow} + H_{X\downarrow} + H_d + V. \tag{H1}$$

The first two terms represent the exciton Hamiltonians for each valley ($\sigma = \uparrow, \downarrow$):

$$H_{X\sigma} = \sum_{\mathbf{K}} \epsilon_{\mathbf{K},X} \hat{X}^\dagger_{\mathbf{K}\sigma} \hat{X}_{\mathbf{K}\sigma} + \sum_{\mathbf{KQ}} \tilde{V}_X(\mathbf{Q}) \hat{X}^\dagger_{\mathbf{K}+\mathbf{Q}\sigma} \hat{X}_{\mathbf{K}\sigma}. \tag{H2}$$

Here, $\hat{X}_{\mathbf{K}\sigma}$ annihilates an exciton of type σ with energy $\epsilon_{\mathbf{K},X} = \epsilon_X + |\mathbf{K}|^2/2m_X$, where m_X is the exciton mass and ϵ_X is the $1s$ exciton energy. The term $\tilde{V}_X$ is the Fourier transform of the exciton moiré potential, which is approximated in real space by [23]

$$V(\mathbf{x}) = \sum_{j=1}^{6} V_j e^{i\mathbf{G}_j \cdot \mathbf{x}}, \tag{H3}$$

where $\mathbf{G}_j$ are the first six reciprocal lattice vectors. The threefold symmetry and the realness of the periodic potential imply that $V_1 = V_3 = V_5$, $V_2 = V_4 = V_6$, and $V_1 = V_4^*$, parametrized by $V_1 = Ve^{i\psi}$, with V determining the potential depth and ψ its shape.

TABLE I. Parameters for electron, hole, and exciton from density functional theory calculations [7]. The mass of the particles is given in units of the bare electron mass m_e. The assumed moiré length is $a_M = 8.2$ nm.

Particle	V (meV)	ψ	m (m_e)
Electron	−6.3	0°	0.45
Hole	1.9	59°	0.55
Exciton	5.6	163°	1

Table I summarizes the relevant parameters for our system as determined by large-scale density functional theory (DFT) calculations [7]. Here, we also include the exciton moiré parameters which are determined by assuming a tightly bound electron-hole pair such that $V_X e^{i\psi_X} \equiv V_e e^{i\psi_e} + V_h e^{i\psi_h}$, where V_i and ψ_i are the moiré parameters for the exciton ($i = X$), electron ($i = e$), and hole ($i = h$).

The third term in the Hamiltonian describes the closed-channel molecule, which mediates interactions between excitons:

$$H_d = \sum_{\mathbf{K}} (\epsilon_{\mathbf{K},d} + \delta_{\mathrm{cc}}) \hat{d}^\dagger_{\mathbf{K}} \hat{d}_{\mathbf{K}} + \sum_{\mathbf{KQ}} 2\tilde{V}_X(\mathbf{Q}) \hat{d}^\dagger_{\mathbf{K}+\mathbf{Q}} \hat{d}_{\mathbf{K}}, \tag{H4}$$

where $\hat{d}_{\mathbf{K}}$ annihilates a closed-channel molecule with energy $\epsilon_{\mathbf{K},d} = 2\epsilon_X + |\mathbf{K}|^2/2M$ ($M = 2m_X$) and detuning δ_{cc}. The closed-channel experiences both exciton potentials, hence the factor of 2 in the moiré potential.

The interactions are mediated according to

$$V = \frac{g}{\sqrt{\mathcal{A}}} \sum_{\mathbf{KQ}} \chi(\mathbf{K}) (\hat{d}^\dagger_{\mathbf{Q}} \hat{X}_{\mathbf{Q}-\mathbf{K},\uparrow} \hat{X}_{\mathbf{K},\downarrow} + \mathrm{H.c.}), \tag{H5}$$

where $\chi(\mathbf{K})$ regularizes the ultraviolet (UV) divergence and $\mathcal{A}$ is the system area. Throughout this section, we use $\chi(\mathbf{K}) = \Theta(\Lambda - |\mathbf{K}|)$, where Λ is the UV cutoff. The bare coupling g and detuning δ_{cc} are renormalized as [73]

$$\frac{\delta_{\mathrm{cc}}}{g^2} = \frac{1}{\mathcal{A}} \sum_{\mathbf{K}} \chi(\mathbf{K}) \frac{1}{E_{\mathrm{BX}} + 2\epsilon_{\mathbf{K},X}}, \tag{H6}$$

with E_{BX} being the energy of the biexciton *without moiré*.

We point out that the two-channel model is equivalent to contact interactions with coupling constant $U = -g^2/\delta_{\mathrm{cc}}$ in the single-channel model limit ($\delta_{\mathrm{cc}}, g \to \infty$). Throughout this work, we exclusively work in the single-channel model limit, since, for our purposes, the two-channel model is used only as a tool to simplify the calculation of the exciton-exciton T matrix.

2. T matrix

To study the interactions we calculate the T matrix, which provides an exact solution to the full two-body problem. To begin, we introduce the free exciton and closed-channel Green's functions:

$$\hat{G}^{(0)}(E) = \frac{1}{E - \hat{H}_{X\uparrow} - \hat{H}_{X,\downarrow}}, \tag{H7}$$

$$\hat{D}^{(0)}(E) = \frac{1}{E - \hat{H}_d}. \tag{H8}$$

The two-body T matrix is given by the infinite series

$$\begin{aligned} T &= \hat{V}\hat{D}^{(0)}\hat{V} + \hat{V}\hat{D}^{(0)}\hat{V}\hat{G}^{(0)}\hat{V}\hat{D}^{(0)}\hat{V} + \cdots \\ &= \hat{V}(\hat{D}^{(0)} + \hat{D}^{(0)}\hat{V}\hat{G}^{(0)}\hat{V}\hat{D}^{(0)} + \cdots)\hat{V} \\ &= \hat{V}\,\hat{D}\,\hat{V}, \end{aligned} \tag{H9}$$

where we suppress the energy dependencies for brevity and $\hat{D}(E)$ is the closed-channel Green's function. Thus, by finding the closed-channel Green's function, we can immediately calculate the T matrix. This approach simplifies the calculation and provides easier access to the biexciton energies, which are both the poles of the T matrix and $\hat{D}(E)$.

The closed-channel Green's function is given by

$$\hat{D}(E) = \frac{1}{[\hat{D}^{(0)}(E)]^{-1} - \frac{g^2}{\mathcal{A}}\hat{\Pi}(E)}, \tag{H10}$$

where we introduce the polarization bubble, which has matrix elements

$$\Pi^{\mathbf{q}}_{\lambda\lambda'} = \sum_{\mathbf{k},\lambda_\uparrow,\lambda_\downarrow} \mathcal{V}^{\mathbf{q},\lambda}_{\mathbf{k}\lambda_\uparrow\lambda_\downarrow} \frac{1}{E - E_{\mathbf{k},\mathbf{q};\lambda_\uparrow,\lambda_\downarrow}} \mathcal{V}^{\mathbf{q},\lambda'*}_{\mathbf{k}\lambda_\uparrow\lambda_\downarrow}, \tag{H11}$$

where $E_{\mathbf{k},\mathbf{q};\lambda_\uparrow,\lambda_\downarrow} \equiv E^{\uparrow}_{\mathbf{q}-\mathbf{k},\lambda_\uparrow} + E^{\downarrow}_{\mathbf{k},\lambda_\downarrow}$ and

$$\mathcal{V}^{\mathbf{q}\lambda_d}_{\mathbf{k}\lambda_\uparrow\lambda_\downarrow} \equiv \langle \mathbf{q}, \lambda_d, d|V|\mathbf{q}-\mathbf{k}, \lambda_\uparrow, \uparrow; \mathbf{k}, \lambda_\downarrow, \downarrow\rangle\sqrt{\mathcal{A}}/g.$$

Here, we introduce a Bloch basis, which satisfies

$$H_{X,\sigma}|\mathbf{k},\lambda,\sigma\rangle = E^{\sigma}_{\mathbf{k},\lambda}|\mathbf{k},\lambda,\sigma\rangle, \tag{H12}$$

$$H_d|\mathbf{k},\lambda,d\rangle = (E^{d}_{\mathbf{k},\lambda} + \delta_{\mathrm{cc}})|\mathbf{k},\lambda,d\rangle, \tag{H13}$$

where $\mathbf{k}$ is the quasimomentum and λ is the band index.

3. Modeling light shifts

Within our model for cross-circular-polarization data, we consider the interaction-induced shift of the probe exciton (denoted by $\uparrow$) by virtual excitons ($\downarrow$) created by the pump. To incorporate the effects of the pump laser, we consider the following modification to the Hamiltonian $\hat{H}_{X\downarrow}$ [30]:

$$\begin{aligned} H_{X\downarrow} = &\sum_{\mathbf{k},\lambda} E^{\downarrow}_{\mathbf{k},\lambda}\hat{X}^{\dagger}_{\mathbf{k},\lambda,\downarrow}\hat{X}_{\mathbf{k},\lambda,\downarrow} + \Omega^* e^{-i\omega_L t}\sum_{\lambda}\phi_{\mathbf{0}}^{(\mathbf{0},\lambda,\downarrow)*}\hat{X}^{\dagger}_{\mathbf{0},\lambda,\downarrow} \\ &+ \Omega e^{i\omega_L t}\sum_{\lambda}\phi_{\mathbf{0}}^{(\mathbf{0},\lambda,\downarrow)}\hat{X}_{\mathbf{0},\lambda,\downarrow}, \end{aligned} \tag{H14}$$

where $\phi_{\mathbf{0}}^{(\mathbf{0},\lambda,\downarrow)} \equiv \langle 0|\hat{X}_{\mathbf{0},\downarrow}|\mathbf{0},\lambda,\downarrow|$ and $\hat{X}_{\mathbf{k},\lambda,\downarrow}$ annihilates a $\downarrow$ exciton with quasimomentum $\mathbf{k}$ and band index λ. Here, Ω represents the light-matter interaction strength; we assume that the light couples only to the zero-momentum exciton and use the rotating wave approximation ($|\epsilon_X - \omega_L| \ll \epsilon_X + \omega_L$). By moving into the rotating frame, it can be seen that the excitons form a coherent state, $|\Phi\rangle = \underline{\hat{D}}(\beta)|0\rangle$ (ignoring normalization), where we introduce the multimode shift operator

$$\underline{\hat{D}}(\beta) = \exp\left[\sum_{\lambda}(\beta_\lambda\hat{X}^{\dagger}_{\mathbf{0},\lambda,\downarrow} - \beta^*_\lambda\hat{X}_{\mathbf{0},\lambda,\downarrow})\right] \tag{H15}$$

and $\beta_\lambda = -\phi_{\mathbf{0}}^{(\mathbf{0},\lambda,\downarrow)*}\Omega^*/(E^{\downarrow}_{\mathbf{0},\lambda} - \omega_L)$.

We can then approximate this energy shift of the λth resonance of the $\uparrow$ probe exciton using the T matrix:

$$\Delta_\lambda(\omega_L) \simeq \sum_{\lambda_\downarrow\lambda'_\downarrow}\beta_{\lambda_\downarrow}T^{\lambda\lambda_\downarrow;\mathbf{0}}_{\lambda\lambda'_\downarrow;\mathbf{0}}(E_{0,\lambda} + \omega_L + 2i\gamma)\beta^*_{\lambda'_\downarrow}, \tag{H16}$$

with $\gamma \approx 1$ meV the inverse lifetime of the exciton. Here, we have the matrix elements of the T matrix defined by

$$T^{\lambda_\uparrow\lambda_\downarrow;\mathbf{0}}_{\lambda'_\uparrow\lambda'_\downarrow;\mathbf{0}}(E) \equiv \langle 0|\hat{X}_{\mathbf{0}\lambda_\downarrow\downarrow}\hat{X}_{\mathbf{0}\lambda_\uparrow\uparrow}\hat{T}(E)\hat{X}^{\dagger}_{\mathbf{0}\lambda'_\uparrow\uparrow}\hat{X}^{\dagger}_{\mathbf{0}\lambda'_\downarrow\downarrow}|0\rangle. \tag{H17}$$

In Eq. (H16), we explicitly include the laser frequency ω_L as a parameter in the self-energy to emphasize its significance: We observe that the laser light shifts the scattering off shell, similar to the effect discussed in the context of polariton-electron scattering [74]. It is important to note that Eq. (H16) captures the ac Stark effect, whereby the shift can change sign when the laser frequency ω_L is tuned into resonance with the biexciton bound state, i.e., $E_{\mathbf{0},\lambda} = \omega_L - E_{\mathrm{BX};\alpha}$, where $E_{\mathrm{BX};\alpha}$ denotes the energy of a zero-quasimomentum biexciton state. However, unlike the simpler case of a monolayer TMD, this sign change does not occur at all biexciton energies, as not all biexciton states couple to the λth exciton mode. We can, therefore, expect that in the experiments, which observe shifts only in the optically active MX_1 and MX_2 modes, it will not be possible to detect all biexciton states.

The magnitude of the shift in Eq. (H16) depends on our choice of $\Omega/\sqrt{\mathcal{A}}$. Since our primary interest is in the zero crossings of the shift (and not its absolute value), we use a simple estimate for this quantity. In particular, we take $\Omega/\sqrt{\mathcal{A}} = \sqrt{2}$ meV/nm, which is chosen to correspond to a reasonable induced exciton density of 5×10^{11} cm^{-2} of $1s$ excitons at a detuning of 20 meV (in the absence of moiré).

4. Same-valley interactions

To conclude our work, we briefly consider interactions from excitons in the same valley, which do not support a bound state. Owing to this, we simply take the Born approximation of the T matrix assuming repulsive contact interactions. Focusing on zero quasimomentum, the interactions between the excitons are given by

$$\hat{\mathscr{V}} = \frac{u_{\mathrm{ex}}}{2} \sum U^{\lambda_1\lambda_2}_{\lambda_3\lambda_4} \hat{X}^\dagger_{\mathbf{0},\lambda_1,\downarrow} \hat{X}^\dagger_{\mathbf{0},\lambda_2,\downarrow} \hat{X}_{\mathbf{0},\lambda_3,\downarrow} \hat{X}_{\mathbf{0},\lambda_4,\downarrow}. \tag{H18}$$

Here, u_{ex} is the strength of the repulsion of two $\mathbf{K} = 0$ excitons (i.e., in the absence of moiré), and we introduce the overlap integral

$$U^{\lambda_1\lambda_2}_{\lambda_3\lambda_4} = \mathcal{A} \int d^2 r \varphi^*_{\lambda_1,\downarrow}(\mathbf{r}) \varphi^*_{\lambda_2,\downarrow}(\mathbf{r}) \varphi_{\lambda_3,\downarrow}(\mathbf{r}) \varphi_{\lambda_4,\downarrow}(\mathbf{r}), \tag{H19}$$

where $\varphi_{\lambda,\downarrow}$ is the Bloch wave function in *real space* at zero quasimomentum with band index λ and valley index $\downarrow$. In order to derive the mean-field Hamiltonian given in the main text, we restrict ourselves to the optically bright excitonic states MX_1 ($\lambda = 0$) and MX_2 ($\lambda = 3$). We furthermore use the fact that $\beta_\lambda/\sqrt{\mathcal{A}} = \kappa_\lambda \sqrt{n_\lambda}$ (with $\kappa_\lambda = e^{i \arg(-\phi_0^{(\mathbf{0},\lambda,\downarrow)*}\Omega^*)}$) and $\langle \Phi | \hat{X}^\dagger_{\mathbf{0},\lambda,\downarrow} \hat{X}_{\mathbf{0},\lambda',\downarrow} | \Phi \rangle = \beta^*_\lambda \beta_{\lambda'}$. Decomposing the interaction in Eq. (H18) using mean-field Hartree-Fock theory then yields Eqs. (1a) and (1b). We point out that, for contact interactions with bosons, the Hartree and Fock terms are identical in magnitude and sign. The relevant overlap integrals are

$$u_{1,1}/u_{\mathrm{ex}} = U^{0,0}_{0,0} = 2.2, \tag{H20a}$$

$$u_{2,2}/u_{\mathrm{ex}} = U^{3,3}_{3,3} = 1.9, \tag{H20b}$$

$$u_{1,2}/u_{\mathrm{ex}} = U^{0,3}_{0,3} = 1.3, \tag{H20c}$$

$$k_1/u_{\mathrm{ex}} = \kappa_0^3 \kappa_3 U^{0,0}_{0,3} = -1.2, \tag{H20d}$$

$$k_2/u_{\mathrm{ex}} = \kappa_0 \kappa_3^3 U^{3,3}_{3,0} = -0.4, \tag{H20e}$$

where we assume that κ are real. All other interaction terms can be derived from these five, since the overlap integral depends only on the number of each index (e.g., $U^{1,1}_{1,0} = U^{1,1}_{0,1} = U^{1,0}_{1,1} = U^{0,1}_{1,1}$).

[1] K. F. Mak and J. Shan, *Semiconductor moiré materials*, Nat. Nanotechnol. **17**, 686 (2022).

[2] E. Y. Andrei, D. K. Efetov, P. Jarillo-Herrero, A. H. MacDonald, K. F. Mak, T. Senthil, E. Tutuc, A. Yazdani, and A. F. Young, *The marvels of moiré materials*, Nat. Rev. Mater. **6**, 201 (2021).

[3] D. M. Kennes, M. Claassen, L. Xian, A. Georges, A. J. Millis, J. Hone, C. R. Dean, D. N. Basov, A. N. Pasupathy, and A. Rubio, *Moiré heterostructures as a condensed-matter quantum simulator*, Nat. Phys. **17**, 155 (2021).

[4] Y. Shimazaki, I. Schwartz, K. Watanabe, T. Taniguchi, M. Kroner, and A. Imamoğlu, *Strongly correlated electrons and hybrid excitons in a moiré heterostructure*, Nature (London) **580**, 472 (2020).

[5] Y. Tang, L. Li, T. Li, Y. Xu, S. Liu, K. Barmak, K. Watanabe, T. Taniguchi, A. H. MacDonald, J. Shan, and K. F. Mak, *Simulation of Hubbard model physics in WSe_2/WS_2 moiré superlattices*, Nature (London) **579**, 353 (2020).

[6] E. C. Regan, D. Wang, C. Jin, M. I. Bakti Utama, B. Gao, X. Wei, S. Zhao, W. Zhao, Z. Zhang, K. Yumigeta *et al.*, *Mott and generalized Wigner crystal states in WSe_2/WS_2 moiré superlattices*, Nature (London) **579**, 359 (2020).

[7] L. Ciorciaro, T. Smoleński, I. Morera, N. Kiper, S. Hiestand, M. Kroner, Y. Zhang, K. Watanabe, T. Taniguchi, E. Demler, and A. İmamoğlu, *Kinetic magnetism in triangular moiré materials*, Nature (London) **623**, 509 (2023).

[8] H. Park, J. Cai, E. Anderson, Y. Zhang, J. Zhu, X. Liu, C. Wang, W. Holtzmann, C. Hu, Z. Liu, T. Taniguchi, K. Watanabe, J.-H. Chu, T. Cao, L. Fu, W. Yao, C.-Z. Chang, D. Cobden, D. Xiao, and X. Xu, *Observation of fractionally quantized anomalous Hall effect*, Nature (London) **622**, 74 (2023).

[9] Y. Zeng, Z. Xia, K. Kang, J. Zhu, P. Knüppel, C. Vaswani, K. Watanabe, T. Taniguchi, K. F. Mak, and J. Shan, *Thermodynamic evidence of fractional Chern insulator in moiré $MoTe_2$*, Nature (London) **622**, 69 (2023).

[10] R. Rapaport, R. Harel, E. Cohen, A. Ron, E. Linder, and L. N. Pfeiffer, *Negatively charged quantum well polaritons in a GaAs/AlAs microcavity: An analog of atoms in a cavity*, Phys. Rev. Lett. **84**, 1607 (2000).

[11] R. A. Suris, *Correlation between trion and hole in Fermi distribution in process of trion photo-excitation in doped QWs*, in *Optical Properties of 2D Systems with Interacting Electrons* (Springer, New York, 2003), pp. 111–124.

[12] M. Sidler, P. Back, O. Cotlet, A. Srivastava, T. Fink, M. Kroner, E. Demler, and A. Imamoglu, *Fermi polaron-polaritons in charge-tunable atomically thin semiconductors*, Nat. Phys. **13**, 255 (2017).

[13] D. K. Efimkin and A. H. MacDonald, *Many-body theory of trion absorption features in two-dimensional semiconductors*, Phys. Rev. B **95**, 035417 (2017).

[14] M. M. Glazov, *Optical properties of charged excitons in two-dimensional semiconductors*, J. Chem. Phys. **153** (2020).

[15] G. Wang, A. Chernikov, M. M. Glazov, T. F. Heinz, X. Marie, T. Amand, and B. Urbaszek, *Colloquium: Excitons in atomically thin transition metal dichalcogenides*, Rev. Mod. Phys. **90**, 021001 (2018).

[16] Y. Xu, S. Liu, D. A. Rhodes, K. Watanabe, T. Taniguchi, J. Hone, V. Elser, K. F. Mak, and J. Shan, *Correlated insulating states at fractional fillings of moiré superlattices*, Nature (London) **587**, 214 (2020).

[17] T. Smoleński, P. E. Dolgirev, C. Kuhlenkamp, A. Popert, Y. Shimazaki, P. Back, X. Lu, M. Kroner, K. Watanabe, T. Taniguchi *et al.*, *Signatures of Wigner crystal of electrons in a monolayer semiconductor*, Nature (London) **595**, 53 (2021).

[18] R. Xiong, J. H. Nie, S. L. Brantly, P. Hays, R. Sailus, K. Watanabe, T. Taniguchi, S. Tongay, and C. Jin, *Correlated insulator of excitons in WSe_2/WS_2 moiré superlattices*, Science **380**, 860 (2023).

[19] B. Gao, D. G. Suárez-Forero, S. Sarkar, T.-S. Huang, D. Session, M. J. Mehrabad, R. Ni, M. Xie, J. Vannucci, S. Mittal, K. Watanabe, T. Taniguchi, A. Imamoglu, Y. Zhou, and M. Hafezi, *Excitonic Mott insulator in a Bose-Fermi-Hubbard system of moiré WS_2/WSe_2 heterobilayer*, Nat. Commun. **15**, 2305 (2024).

[20] Z. Lian, Y. Meng, L. Ma, I. Maity, L. Yan, Q. Wu, X. Huang, D. Chen, X. Chen, X. Chen, M. Blei, T. Taniguchi, K. Watanabe, S. Tongay, J. Lischner, Y.-T. Cui, and S.-F. Shi, *Valley-polarized excitonic Mott insulator in* WS_2/WSe_2 *moiré superlattice*, Nat. Phys. **20**, 34 (2023).

[21] H. Park, J. Zhu, X. Wang, Y. Wang, W. Holtzmann, T. Taniguchi, K. Watanabe, J. Yan, L. Fu, T. Cao, D. Xiao, D. R. Gamelin, H. Yu, W. Yao, and X. Xu, *Dipole ladders with large Hubbard interaction in a moiré exciton lattice*, Nat. Phys. **19**, 1286 (2023).

[22] B.-H. Lin, Y.-C. Chao, I.-T. Hsieh, C.-P. Chuu, C.-J. Lee, F.-H. Chu, L.-S. Lu, W.-T. Hsu, C.-W. Pao, C.-K. Shih *et al.*, *Remarkably deep moiré potential for intralayer excitons in* $MoSe_2/MoS_2$ *twisted heterobilayers*, Nano Lett. **23**, 1306 (2023).

[23] F. Wu, T. Lovorn, and A. H. MacDonald, *Topological exciton bands in moiré heterojunctions*, Phys. Rev. Lett. **118**, 147401 (2017).

[24] S. Brem, C. Linderälv, P. Erhart, and E. Malic, *Tunable phases of moiré excitons in van der Waals heterostructures*, Nano Lett. **20**, 8534 (2020).

[25] M. H. Naik, E. C. Regan, Z. Zhang, Y.-H. Chan, Z. Li, D. Wang, Y. Yoon, C. S. Ong, W. Zhao, S. Zhao *et al.*, *Intralayer charge-transfer moiré excitons in van der Waals superlattices*, Nature (London) **609**, 52 (2022).

[26] T.-S. Huang, P. Lunts, and M. Hafezi, *Nonbosonic moirémoiré excitons*, Phys. Rev. Lett. **132**, 186202 (2024).

[27] H. Guo, X. Zhang, and G. Lu, *Shedding light on moiré excitons: A first-principles perspective*, Sci. Adv. **6**, abc5638 (2020).

[28] P. D. Cunningham, A. T. Hanbicki, T. L. Reinecke, K. M. McCreary, and B. T. Jonker, *Resonant optical Stark effect in monolayer* WS_2, Nat. Commun. **10**, 5539 (2019).

[29] A. O. Slobodeniuk, P. Koutenský, M. Bartoš, F. Trojánek, P. Malý, T. Novotný, and M. Kozák, *Ultrafast valley-selective coherent optical manipulation with excitons in* WSe_2 *and* MoS_2 *monolayers*, npj 2D Mater. Appl. **7**, 17 (2023).

[30] M. Combescot, *Semiconductors in strong laser fields: From polariton to exciton optical Stark effect*, Phys. Rep. **221**, 167 (1992).

[31] S. Schmitt-Rink and D. S. Chemla, *Collective excitations and the dynamical Stark effect in a coherently driven exciton system*, Phys. Rev. Lett. **57**, 2752 (1986).

[32] R. Zimmermann, *On the dynamical Stark effect of excitons. The low-field limit*, Phys. Status Solidi **146(b)**, 545 (2006).

[33] H. Haug and S. W. Koch, *Quantum Theory of the Optical and Electronic Properties of Semiconductors* (World Scientific, Singapore, 2009).

[34] T. Uto, B. Evrard, K. Watanabe, T. Taniguchi, M. Kroner, and A. İmamoğlu, *Interaction-induced ac Stark shift of exciton-polaron resonances*, Phys. Rev. Lett. **132**, 056901 (2024).

[35] S. Sarkar, M. J. Mehrabad, D. G. Suárez-Forero, L. Gu, C. J. Flower, L. Xu, K. Watanabe, T. Taniguchi, S. Park, H. Jang, Y. Zhou, and M. Hafezi, *Sub-wavelength optical lattice in 2d materials*, arXiv:2406.00464.

[36] C.-K. Yong, J. Horng, Y. Shen, H. Cai, A. Wang, C.-S. Yang, C.-K. Lin, S. Zhao, K. Watanabe, T. Taniguchi *et al.*, *Biexcitonic optical Stark effects in monolayer molybdenum diselenide*, Nat. Phys. **14**, 1092 (2018).

[37] E. J. Sie, C. H. Lui, Y.-H. Lee, J. Kong, and N. Gedik, *Observation of intervalley biexcitonic optical Stark effect in monolayer* WS_2, Nano Lett. **16**, 7421 (2016).

[38] K. Hao, J. F. Specht, P. Nagler, L. Xu, K. Tran, A. Singh, C. K. Dass, C. Schüller, T. Korn, M. Richter *et al.*, *Neutral and charged inter-valley biexcitons in monolayer* $MoSe_2$, Nat. Commun. **8**, 15552 (2017).

[39] P. D. Cunningham, A. T. Hanbicki, T. L. Reinecke, K. M. McCreary, and B. T. Jonker, *Resonant optical Stark effect in monolayer* WS_2, Nat. Commun. **10**, 5539 (2019).

[40] H. N. Cam, N. T. Phuc, and V. A. Osipov, *Symmetry-dependent exciton-exciton interaction and intervalley biexciton in monolayer transition metal dichalcogenides*, npj 2D Mater. Appl. **6**, 22 (2022).

[41] S. Brem and E. Malic, *Optical signatures of moiré trapped biexcitons*, 2D Mater. **11**, 025030 (2024).

[42] Recent work has shown that the lowest-energy moiré exciton resonances can indeed be characterized as 1*s* excitons [25].

[43] C. Ciuti, V. Savona, C. Piermarocchi, A. Quattropani, and P. Schwendimann, *Role of the exchange of carriers in elastic exciton-exciton scattering in quantum wells*, Phys. Rev. B **58**, 7926 (1998).

[44] V. Shahnazaryan, I. Iorsh, I. A. Shelykh, and O. Kyriienko, *Exciton-exciton interaction in transition-metal dichalcogenide monolayers*, Phys. Rev. B **96**, 115409 (2017).

[45] B. Polovnikov, J. Scherzer, S. Misra, X. Huang, C. Mohl, Z. Li, J. Göser, J. Förste, I. Bilgin, K. Watanabe *et al.*, *Coulomb-correlated states of moiré excitons and elementary charges on a semiconductor moiré lattice at integer and fractional fillings*, arXiv:2208.04056.

[46] L. B. Tan, O. K. Diessel, A. Popert, R. Schmidt, A. Imamoglu, and M. Kroner, *Bose polaron interactions in a cavity-coupled monolayer semiconductor*, Phys. Rev. X **13**, 031036 (2023).

[47] N. Kiper, H. S. Adlong, A. Christianen, M. Kroner, K. Watanabe, T. Taniguchi, and A. Imamoglu, *Confined trions and Mott-Wigner states in a purely electrostatic moiré potential*, Phys. Rev. X **15**, 011049 (2025).

[48] L. B. Tan, O. Cotlet, A. Bergschneider, R. Schmidt, P. Back, Y. Shimazaki, M. Kroner, and A. İmamoğlu, *Interacting polaron-polaritons*, Phys. Rev. X **10**, 021011 (2020).

[49] D. Huang, J. Choi, C.-K. Shih, and X. Li, *Excitons in semiconductor moiré superlattices*, Nat. Nanotechnol. **17**, 227 (2022).

[50] L. Du, M. R. Molas, Z. Huang, G. Zhang, F. Wang, and Z. Sun, *Moiré photonics and optoelectronics*, Science **379**, eadg0014 (2023).

[51] N. Zhang, A. Surrente, M. Baranowski, D. K. Maude, P. Gant, A. Castellanos-Gomez, and P. Plochocka, *moiré intralayer excitons in a* $MoSe_2/MoS_2$ *heterostructure*, Nano Lett. **18**, 7651 (2018).

[52] C. Jin, E. C. Regan, A. Yan, M. Iqbal Bakti Utama, D. Wang, S. Zhao, Y. Qin, S. Yang, Z. Zheng, S. Shi *et al.*, *Observation of moiré excitons in* WSe_2/WS_2 *heterostructure superlattices*, Nature (London) **567**, 76 (2019).

[53] E. Liu, E. Barré, J. van Baren, M. Wilson, T. Taniguchi, K. Watanabe, Y.-T. Cui, N. M. Gabor, T. F. Heinz, Y.-C. Chang *et al.*, *Signatures of moiré trions in* $WSe_2/MoSe_2$ *heterobilayers*, Nature (London) **594**, 46 (2021).

[54] B. Wu, H. Zheng, S. Li, J. Ding, J. He, Y. Zeng, K. Chen, Z. Liu, S. Chen, A. Pan *et al.*, *Evidence for moiré intralayer excitons in twisted* WSe_2/WSe_2 *homobilayer superlattices*, Light Sci. Appl. **11**, 166 (2022).

[55] K. Tran *et al.*, *Evidence for moiré excitons in van der Waals heterostructures*, Nature (London) **567**, 71 (2019).

[56] E. M. Alexeev, D. A. Ruiz-Tijerina, M. Danovich, M. J. Hamer, D. J. Terry, P. K. Nayak, S. Ahn, S. Pak, J. Lee, J. I. Sohn *et al.*, *Resonantly hybridized excitons in moiré superlattices in van der Waals heterostructures*, Nature (London) **567**, 81 (2019).

[57] K. L. Seyler, P. Rivera, H. Yu, N. P. Wilson, E. L. Ray, D. G. Mandrus, J. Yan, W. Yao, and X. Xu, *Signatures of moiré-trapped valley excitons in* $MoSe_2/WSe_2$ *heterobilayers*, Nature (London) **567**, 66 (2019).

[58] E. Anderson, J. Cai, A. P. Reddy, H. Park, W. Holtzmann, K. Davis, T. Taniguchi, K. Watanabe, T. Smolenski, A. Imamoğlu, T. Cao, D. Xiao, L. Fu, W. Yao, and X. Xu, *Trion sensing of a zero-field composite Fermi liquid*, Nature (London) **635**, 590 (2024).

[59] H. Yu, G.-B. Liu, J. Tang, X. Xu, and W. Yao, *Moiré excitons: From programmable quantum emitter arrays to spin-orbit–coupled artificial lattices*, Sci. Adv. **3**, 1701696 (2017).

[60] D. Fausti, R. I. Tobey, N. Dean, S. Kaiser, A. Dienst, M. C. Hoffmann, S. Pyon, T. Takayama, H. Takagi, and A. Cavalleri, *Light-induced superconductivity in a stripe-ordered cuprate*, Science **331**, 189 (2011).

[61] C. Piermarocchi, P. Chen, L. J. Sham, and D. G. Steel, *Optical RKKY interaction between charged semiconductor quantum dots*, Phys. Rev. Lett. **89**, 167402 (2002).

[62] J. Fernández-Rossier, C. Piermarocchi, P. Chen, A. H. MacDonald, and L. J. Sham, *Coherently photoinduced ferromagnetism in diluted magnetic semiconductors*, Phys. Rev. Lett. **93**, 127201 (2004).

[63] X. Wang, C. Xiao, H. Park, J. Zhu, C. Wang, T. Taniguchi, K. Watanabe, J. Yan, D. Xiao, D. R. Gamelin, W. Yao, and X. Xu, *Light-induced ferromagnetism in moiré superlattices*, Nature (London) **604**, 468 (2022).

[64] See https://www.research-collection.ethz.ch/handle/20.500.11850/661389.

[65] P. Zomer, M. Guimarães, J. Brant, N. Tombros, and B. Van Wees, *Fast pick up technique for high quality heterostructures of bilayer graphene and hexagonal boron nitride*, Appl. Phys. Lett. **105**, 013101 (2014).

[66] G. Scuri, Y. Zhou, A. A. High, D. S. Wild, C. Shu, K. De Greve, L. A. Jauregui, T. Taniguchi, K. Watanabe, P. Kim *et al.*, *Large excitonic reflectivity of monolayer* $MoSe_2$ *encapsulated in hexagonal boron nitride*, Phys. Rev. Lett. **120**, 037402 (2018).

[67] A. Laturia, M. L. Van de Put, and W. G. Vandenberghe, *Dielectric properties of hexagonal boron nitride and transition metal dichalcogenides: From monolayer to bulk*, npj 2D Mater. Appl. **2**, 6 (2018).

[68] K. K. Kim, A. Hsu, X. Jia, S. M. Kim, Y. Shi, M. Dresselhaus, T. Palacios, and J. Kong, *Synthesis and characterization of hexagonal boron nitride film as a dielectric layer for graphene devices*, ACS Nano **6**, 8583 (2012).

[69] F. Barachati, A. Fieramosca, S. Hafezian, J. Gu, B. Chakraborty, D. Ballarini, L. Martinu, V. Menon, D. Sanvitto, and S. Kéna-Cohen, *Interacting polariton fluids in a monolayer of tungsten disulfide*, Nat. Nanotechnol. **13**, 906 (2018).

[70] T. Smoleński, O. Cotlet, A. Popert, P. Back, Y. Shimazaki, P. Knüppel, N. Dietler, T. Taniguchi, K. Watanabe, M. Kroner, and A. Imamoglu, *Interaction-induced Shubnikov–de Haas oscillations in optical conductivity of monolayer* $MoSe_2$, Phys. Rev. Lett. **123**, 097403 (2019).

[71] J. B. Muir, J. Levinsen, S. K. Earl, M. A. Conway, J. H. Cole, M. Wurdack, R. Mishra, D. J. Ing, E. Estrecho, Y. Lu *et al.*, *Interactions between Fermi polarons in monolayer* WS_2, Nat. Commun. **13**, 6164 (2022).

[72] H. S. Adlong, J. Levinsen, and M. M. Parish, *Microscopic theory of the Hubbard interaction in low-dimensional optical lattices*, Phys. Rev. A **111**, 033307 (2025).

[73] J. Levinsen and M. M. Parish, *Strongly interacting two-dimensional Fermi gases*, Annu. Rev. Cold At. Mol. **3**, 1 (2015).

[74] S. S. Kumar, B. C. Mulkerin, M. M. Parish, and J. Levinsen, *Trion resonance in polariton-electron scattering*, Phys. Rev. B **108**, 125416 (2023).